Master's Thesis

Dual-doped mesoporous carbon/SWCNT nanoshells for Li-ion battery electrode materials

Ye-Ri Jang

Department of Energy Engineering

(Battery Science and Technology)

Graduate School of UNIST

2017

Dual-doped mesoporous carbon/SWCNT nanoshells

for Li-ion battery electrode materials

Ye-Ri Jang

Department of Energy Engineering

(Battery Science and Technology)

Graduate School of UNIST

Dual-doped mesoporous carbon/SWCNT
nanoshells for Li-ion battery electrode materials

A thesis/dissertation

submitted to the Graduate School of UNIST

in partial fulfillment of the

requirements for the degree of

Master of Science

Ye-Ri Jang

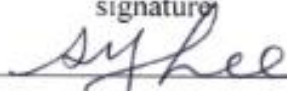12. 14. 2016 Month/Day/Year of submission

Approved by
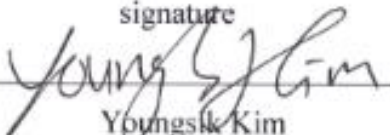
_____

Advisor

Sang-Young Lee

Dual-doped mesoporous carbon/SWCNT nanoshells for Li-ion battery electrode materials
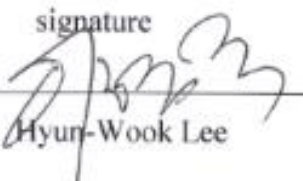
Ye-Ri Jang

This certifies that the thesis/dissertation of Ye-Ri Jang is approved.

12. 14. 2016 Month/Day/Year of submission

signature

Advisor: Sang-Young Lee

signature

Youngsik Kim

signature

Hyun-Wook Lee

Abstract

There is no doubt that rechargeable lithium-ion batteries (LIBs) have been developed as an electrical power source in a wide variety of energy storage systems including portable electronics, electric vehicles (EVs) and plug-in hybrid electric vehicle (PHEVs). Continuous advanced demands for higher energy density energy storage systems strongly push us to develop breakthroughs for improved cathode materials of LIBs. Recently, over-lithiated layered metal oxides ($xLi_2MnO_3 \cdot (1-x)LiMO_2$, [M=Ni, Co, Mn], OLOs) materials, which are widely used in cathode materials of LIBs for high discharge capacity (over 250 mAh/g), are struggling with fast capacity fading and Mn dissolution on the unstable lithium-rich layered metal oxides surface. The poor electrical conductivity of lithium-rich layered metal oxides and Mn dissolution-triggered by-products are known to induce serious capacity fading during charge/discharge cycling.

As a newly-synthesized polymeric ionic liquid (PIL)-driven material/single-walled carbon nanotube (SWCNT) nano-architecture strategy to develop an ion/electron-conductive nanoshells far beyond traditional surface modification, we have demonstrated single-walled carbon nanotube (SWCNT)-embedded and dual atom (nitrogen (N) and sulfur (S))-doped mesoporous carbon shells (referred to as "SMC" shell) on the LNMO ($LiNi_{0.5}Mn_{1.5}O_4$) as well as OLO ($0.49Li_2MnO_3 \cdot 0.51LiNi_{0.37}Co_{0.24}Mn_{0.39}O_2$) surface. The SMC-coated electrode materials are fabricated *via* simple mixing of pristine active materials in the SWCNT/PIL mixture solution and the subsequent one-pot carbonization process of the coated PIL on active materials surface. The PIL synthesized herein consists of poly(1-vinyl-3-ethylimidazolium) cations and dodecyl sulfate counter anions, of which chemical structures are purposeful designed to achieve multifunctional roles as: i) precursor of conformal/continuous carbon shell, ii) dual (N and S)-doping source, iii) porogen, and iv) SWCNT dispersant. Driven by such chemical/structural originality, the SMC effectively reduces unwanted interfacial side reactions between the cathode materials and liquid electrolyte while charge/discharge process. As a consequence, the SMC-coated cathode materials provided unprecedented improvements in the high-performance (rate capability, cycling performance and thermal stability) of lithium-ion batteries.

The SMC-coated cathode materials hold a great deal of promise as a facile and versatile platform surface modification technology for high-performance batteries and also open a new opportunity for next-generation multifunctional molecularly-designed, ion/electron-conductive nanoshells on electrode materials that are in strong pursuit of progress in electrochemical performance.

Contents

List of Figures

with initial concentration of 2.0 mg mL^{-1}. Yellow arrows indicate the thick and irregularly-deposited MC shell on the OLO surface.

Figure 12. PVIm[DS]-assisted dispersion of SWCNTs and structural characterization of OLO@SMC. (A) (Top) Photographs of SWCNT/DMAc suspensions incorporating PVIm[Br], SDS, and PVIm[DS]. (Bottom) Schematic illustration depicting the advantageous effect of PVIm[DS] on the SWCNT dispersion (i.e., synergistic effect of PVIm$^+$ cations and DS$^-$ anions). (B) vis-NIR absorption spectra of SWCNT/DMAc suspension incorporating PVIm[Br], SDS, and PVIm[DS], wherein the samples were subjected to centrifugation (10,000 g) and the supernatant solutions were collected exclusively for this characterization. (C) SEM images of OLO powders coated with SWCNT/PVIm[DS] coating solution. (D) SEM (left) and HRTEM (right) images of OLO@SMC. The SWCNTs embedded in the MC shells were marked with yellow circles. (E) Conceptual illustration depicting the structural uniqueness of SMC shells and their contribution to the ion/electron transport phenomena.

Figure 13. XRD patterns of the pristine OLO and OLO@SMC powders.

Figure 14. Effect of OLO@SMC on the electrochemical performance of coin (2032-type) cells. (A) Discharge rate capability of pristine OLO, OLO@MC, and OLO@SMC, wherein the cells were charged at a constant current density of 0.2 C (0.34 mA cm^{-2}) and discharged at various current densities ranging from 0.2 to 5.0 C. (B) (Left) GITT profiles of the cells assembled with pristine OLO and OLO@SMC cathodes. (Right) Change in internal cell resistances as a function of state of charge (SOC) and depth of discharge (DOD). (C) Comparison of cycling performance (at charge/discharge current density = 3.0 C/3.0 C under voltage range of of 2.0–4.7 V) between pristine OLO, OLO@MC, and OLO@SMC. (D)–(G) Analysis of cells (OLO vs OLO@SMC) after cycling test (50 cycles): (D) SEM image of OLO@SMC cathode. The inset shows the morphology of the OLO cathode. (E) XPS F 1s spectra of the OLO and OLO@SMC cathodes. (F) TOF-SIMS images of the LiF byproducts formed on the OLO and OLO@SMC cathodes. (G) ICP-OES results showing the amount of metallic Mn deposited on the Li metal anodes assembled with the OLO and OLO@SMC cathodes. (H) DSC thermograms showing interfacial exothermic reaction between delithiated (charged to 4.7 V) OLO cathodes and liquid electrolyte.

Figure 15. Charge/discharge profiles (for 1st and 50th cycles) of the pristine OLO, OLO@MC, and OLO@SMC cathodes, wherein the cells were cycled at charge/discharge current density = 3.0 C/3.0 C under voltage range of 2.0 – 4.7 V.

Figure 16. Application of SMC shells to high-voltage LNMO cathode materials. (A) SEM image of LNMO@SMC, wherein the SWCNTs embedded in the MC shells were marked with yellow circles. The inset shows the morphology of pristine LNMO. (B) Electrical conductivity of pristine LNMO and LNMO@SMC. (C) Discharge rate capability of pristine LNMO and LNMO@SMC, wherein the cells were charged at a constant current density of 0.2C and discharged at various current densities ranging from 0.2 to 10.0C. (D) DSC thermograms showing the interfacial exothermic reaction between the delithiated (charged to 4.95 V) LNMO cathodes and liquid electrolyte.

List of Table

CHAPTER I. INTRODUCTION

1.1. Operating principle of lithium-ion batteries

Lithium-ion batteries (LIBs) are currently being developed to fulfill high power for many energy storage applications regarding portable electrical devices, electric vehicles (EVs), plug-in hybrid electric vehicles (PHEVs) and grid-scale energy storage systems (ESSs). Also, LIBs essentially require reliable electrochemical properties, because they possess serious performance deterioration problems such as thermal instability, voltage drop, poor rate capability and decreasing energy density during cycling[1].

Conventional LIBs consist of four specific components, i.e., a positive electrode (cathode), a negative electrode (anode) divided by a separator and electrolyte which enable ion transfer (Figure 1). In the charging process, lithium ions migrate through a separator across the electrolyte from the cathode to the anode and the electrons move through the external circuit (Equation 1). During the battery discharging process, lithium ions transfer from the anode to the cathode across the electrolyte (Equation 2). For instance, using conventional rechargeable LIBs, the $LiCoO_2$ cathodes and graphite anodes have been described in the equations below[2-3].

$$\text{Cathode side: } LiCoO_2 \leftrightarrows Li_{1-x}CoO_2 + xLi^+ + xe^- \quad (1)$$

$$\text{Anode side: } xLi^+ + xe^- + xC_6 \leftrightarrows xLiC_6 \quad (2)$$

$$\text{Total reaction: } LiCoO_2 + xC_6 \leftrightarrows Li_{1-x}CoO_2 + xLiC_6 \quad (3)$$
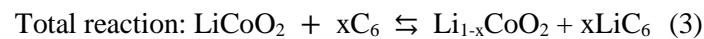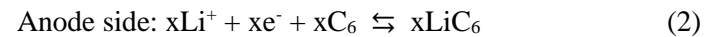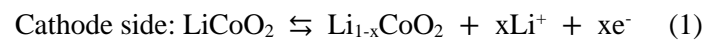
$$(\rightarrow: \text{Charge reaction}, \ \leftarrow: \text{Discharge reaction})$$
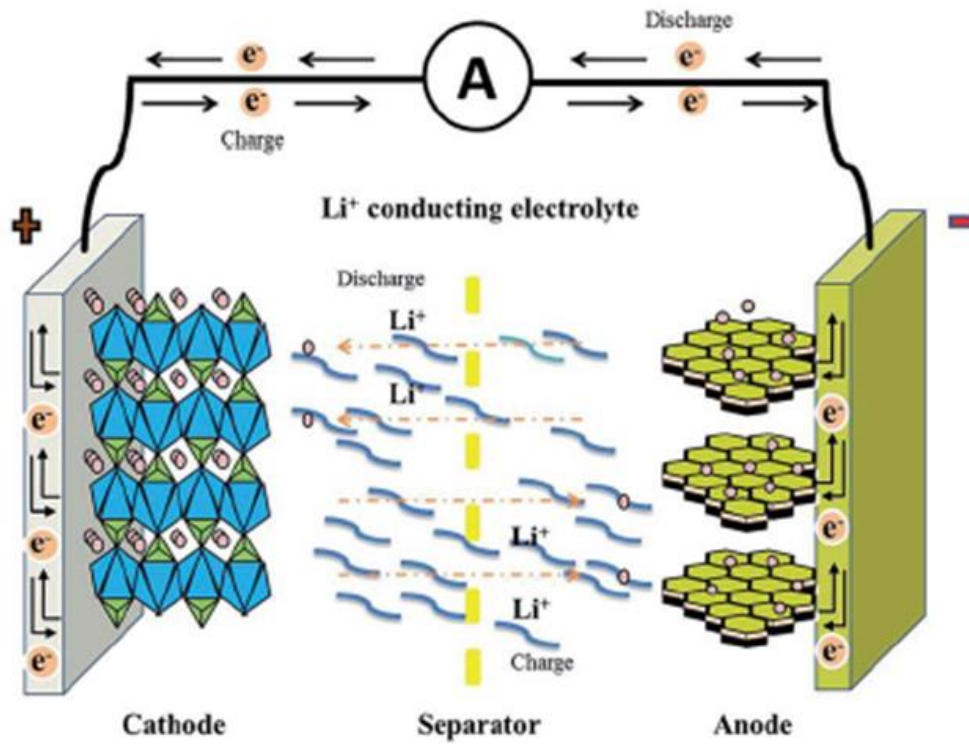
Figure 1. A schematic diagram of representative lithium-ion batteries: Cathode, Anode, Electrolyte and Separator.

Recently, endless demands for higher energy density and low cost push us to substitute commercial $LiCoO_2$ (LCO) to alternative active materials. Layered-type lithium-rich transition-metal oxides, so-called over-lithiated layered oxides (OLOs), have received great attention as one of the most prospective candidates due to their high capacities over 200 mAh g^{-1} as well as their low cost and environmentally friendly property[4]. However, inherent poor rate capability and rapid capacity fading, which mainly results from the low electrical conductivity ($\sim 10^{-9}$ S cm^{-1}) and undesired side reactions on the unstable Li-rich outermost surface, pose the most critical challenge of securing sustainable electrochemical performance in LIBs[5].

Enormous efforts have been undertaken to overcome the problems mentioned above. Nanostructured OLOs provide reduced diffusion paths of Li^+ ions and enlarge interfacial reaction sites between the OLO and electrolytes[6-8], however, the largely exposed surface also labilizes the nano-sized OLOs[8]. Elemental doping could be an effective approach to improve the electrical conductivity and reduce the electrochemical impedance[9-12]. Furthermore, surface modifications have been established as one of the most powerful tools to overcome the intrinsic shortcomings of the OLO[13-16]. The inorganic[13-14] and organic[15-16] material-coated layer works as a protective layer against side reactions, leading to considerable improvements in electrochemical performances as well as thermal stability, due to the alleviated direct contact between the OLO surface and electrolytes[5]. In addition, with an aim to increase facilitated ion/electron conduction, mesoporous carbons have been extensively investigated for the surface modification[17-19], however, the insufficient electrical conductivity of carbon layers demands further advances in material/structural designs constantly.

1.2. General requirements for battery cathodes

Among Lithium-Ion Batteries (LIBs) compositions, cathode materials are demanded for excellent cycling stability, high rate capability and high energy density. Recently, newly developed cathode materials that are chemically modified through atomic or molecular engineering would provide considerably enhanced properties for energy storage systems. However, LIBs power density is still relatively low due to large polarization caused by low lithium diffusion rate in the cathode material during the charge/discharge process. To overcome polarization, cathode materials which have short diffusion distance and large surface area should be designed and fabricated for enhanced electrical conduction and ionic transportation. Moreover, the fundamental requirements for ideal cathode materials in LIBs are as follows.

(1) Stability (Prevention of degradation and structural change. The host structure should not change during intercalation/deintercalation process).

(2) Fast reaction with lithium during intercalation/deintercalation process.

(3) Excellent electronic conductivity (allowing free electron movement within the material during electro-chemical reactions and enhancing the overall energy density by minimizing the necessity for inactive conductive diluents).

(4) Low cost.

(5) Environmental-friendly.

Also, the Faradaic reactions related to energy storage occurs on the electrode surface, in which charge and mass transfer reactions are involved with the electrode; therefore, the transport distance and large surface area play significant roles in determining the battery performance (i.e. cyclic and rate stability) along with inducing structural durability for volume change that accompanies lithium intercalation/deintercalation[20-21].

CHAPTER II. DUAL-DOPED MESOPOROUS CARBON/SWCNT NANOSHELLS FOR HIGH-PERFORMANCE BATTERY CATHODES

2.1. Introduction

The forthcoming ubiquitous energy era, which will involve widespread use of smart portable devices, internet of things (IOTs), and electric vehicles (EVs), has driven a relentless pursuit of high-energy density/high-safety rechargeable energy storage systems with reliable electrochemical performance[22-24]. Among the numerous power sources reported to date, lithium-ion batteries (LIBs) are undoubtedly positioned as a compelling electrochemical system to meet these stringent demands[3, 25]. To promote sustainable development and to extend the applications of LIBs, tremendous efforts have been devoted to synthesizing and engineering electrochemically active components such as electrode materials and electrolytes, which play crucial roles in governing the redox reaction in cells[26-28].

Formidable challenges facing LIBs involve performance deterioration and safety failures that occur during repeated charge/discharge cycling, which are known to mostly arise from electrode–electrolyte interface issues[27-28]. In particular, unwanted side reactions, including byproduct generation, metal-ion dissolution, and exothermic reactions, often occur at the electrode–electrolyte interface, resulting in significant loss of electrochemical capacity and cell safety. Recently, high-capacity (e.g., over-lithiated layered oxide (OLO, $0.49Li_2MnO_3 \cdot 0.51LiNi_{0.37}Co_{0.24}Mn_{0.39}O_2$)[29-30]) and high-voltage (e.g., spinel-type oxide (LNMO, $LiNi_{0.5}Mn_{1.5}O_4$)[31-32]) cathode materials have garnered great attention as attractive candidates for realizing high-energy (energy = capacity × voltage) density cells. However, safety concerns with the electrode–electrolyte interface tend to become more serious with these high-capacity/high-voltage cathode materials because of their vigorous surface reactivity and structural instability.

A vast variety of research has striven to resolve the electrode–electrolyte interface problems, most of which focused on electrolyte additive[16, 33-34], elemental doping[35-37], and surface modification[38-41] of electrode materials. In particular, covering the surface of cathode materials with a thin layer is known to effectively suppress their direct contact with electrolytes, thus mitigating unwanted interfacial side reactions. An ideal coating layer for electrode materials should provide high surface coverage (as a protective layer) and facilitate ion/electron transport (as an ion/electron conduction channel). However, most previous results failed to completely fulfill these requirements.

Mesoporous carbons have attracted significant attention as a new coating substance for catalysts and as carbon electrode materials for LIBs, supercapacitors, and lithium-sulfur batteries[17-19]. However, mesoporous carbon shells require complicated and multiple synthetic steps for constructing their unique porous structure. Moreover, although a mesoporous structure is achieved (which allows ion transport), such carbon shells suffer from insufficient electronic conductivity. These drawbacks have prevented the application extension of mesoporous carbon shells. Meanwhile, polymeric ionic liquids (PILs),

which are defined as polymeric cations/counter anions or polymeric anions/counter cations (or polyzwitterions), have been extensively investigated for use in solid-state polyelectrolytes[42-44]. In addition, PILs have recently been explored as an alternative precursor of conductive carbons[45-47], a heteroatom doping source[45], and a polymeric dispersant of carbon nanotubes[48].

Here, as a PIL-mediated interfacial control strategy to address the long-standing challenges of electrode-electrolyte instability, we demonstrate a new class of molecularly-designed, ion/electron-conductive nanoshields based on single-walled carbon nanotube (SWCNT)-embedded, dual (N and S)-doped mesoporous carbon (referred to as "SMC") shells for LIB electrode materials. We choose OLO as a high-capacity cathode material and LNMO as a high-voltage cathode material as model cathode materials to explore the feasibility and practical applicability of the proposed nanoshield concept. The SMC shell is formed on cathode materials through solution deposition of the SWCNT/PIL mixture and subsequent carbonization.

2.2. Experimental

Materials

SWCNTs (EC-P, purity > 99%, diameter 1.7−2.1 nm) were purchased from Meijo Nano Carbon Co., Ltd. Bromoethane (98%), 1-vinylimidazole (99%), and sodium dodecyl sulfate (99%) were purchased from Sigma-Aldrich, methanol (>99.8%), *N,N*-dimethylacetamide (DMAc) (>99.5%), and 1-methyl-2-pyrrolidone (NMP) (>99.7%) were obtained from DAEJUNG Chemicals & Metals Co., Ltd. Chloroform (99.5%) and α,α′-azoisobutyronitrile (98%) were purchased from Samchun Pure Chemical Co., Ltd. and Junsei Chemical Co., Ltd., respectively. All these chemicals were used as received.

2.2.1. Synthesis of PVIm[DS]

First, poly(1-vinyl-3-ethylimidazolium) bromide (referred to as "PVIm[Br]") was synthesized via the traditional radical polymerization[49-50]. Bromoethane (40 g) was added to 1-vinylimidazole (20 g) under stirring at room temperature. Next, the white precipitate (i.e., 1-vinyl-3-ethylimidazolium bromide (referred to as "VIm[Br]")) was collected through vacuum filtration and rinsed with ethyl acetate. Then, VIm[Br] monomer (27 g) in chloroform (270 mL) was polymerized at 60 °C for 2 h, wherein α,α′-azoisobutyronitrile (AIBN; 0.54 g) was used as an initiator. The yellowish-white solids were collected after rinsing with chloroform. Meanwhile, the PVIm[DS] was obtained using a modified anion exchange method[49-50]. SDS (20 g) solution (200 mL) was added to the PVIm[Br] (10 g) solution (200 mL) under stirring at room temperature, resulting in the precipitation of white solid powders.

2.2.2. Synthesis of dual-doped mesoporous carbon shells on cathode particles

The dual (N and S)-doped mesoporous carbon shell was formed on the OLO powders via the following procedures. The as-synthesized PVIm[DS] (5, 20, 50, and 100 mg) powders were dissolved in DMAc (50 mL) at 60 °C for 2 h. Into the PVIm[DS] solution, 1 g of OLO powders were added. After stirring for 20 h, the PVIm[DS]-deposited OLO powders were collected using a PTFE membrane filter (pore size ~ 0.45 μm) after vacuum drying at 120 °C, and then heated to 600 °C at a rate of 5 °C min^{-1} under an Ar atmosphere in a tube furnace. After carbonization at 600 °C for 2 h, the black powders were obtained.

2.2.3. Synthesis of SWCNT-embedded, dual-doped mesoporous carbon shells

The SWCNTs (1 mg) were mixed for 3 h with PVIm[DS] (50 mg) in DMAc (50 mL) using a sonicator. Subsequently, 1 g of OLO (or LNMO) powders were added and further mixed using an orbital shaker for 20 h. The SWCNT/PVIm[DS]-deposited OLO (or LNMO) powders were collected and then subjected to the same carbonization process as that used for the dual-doped mesoporous carbon shells described above.

2.2.4. Characterizations

The Scanning electron microscopy (SEM) and high-resolution transmission electron microscopy (HRTEM) characterization methods were carried out using an S-4800 (HITACHI, Japan) at 5 kV and a JEM-2100F (JEOL, Japan) at 100 kV, respectively. Thermogravimetric analysis (TGA) was conducted using a Q500 (TA Instruments, USA) under an ambient atmosphere by heating to 900 $^{\circ}$C at the rate of 5 $^{\circ}$C min^{-1}. The differential scanning calorimetry (DSC) measurement was performed using a Q200 (TA Instruments, USA). The Fourier transform infrared (FT-IR) and Raman spectra were obtained using a Varian 660-IR (Varian Medical systems, Inc., USA) and an Alpha 300S (WITec, Germany) with a 532 nm laser, respectively. The specific surface areas were analyzed based on nitrogen adsorption-desorption measurements at 77 K using a physisorption analyzer ASAP2020 (Micromeritics, USA), and pore size distributions were determined by exploiting the density functional theory (DFT) method applied to the adsorption branch of the isotherm. The X-ray photoelectron spectroscopy (XPS) and x-ray diffraction (XRD) analysis were conducted using a K-Alpha™$^{+}$ XPS system (Thermo Scientific™, USA) and a D8 Advance (Bruker, Germany) in the range of $10^{\circ} < 2\theta < 90^{\circ}$ at 40 kV and 40 mA (Cu Kα radiation, $\lambda = 0.154$ nm). The visible-near-infrared (vis-NIR) spectra were measured using an OPTIZEN α (Mecasys, Korea).

2.2.5. Electrochemical analysis and application to Li-ion cells

The cathodes were fabricated by casting NMP-based slurries (cathode materials/carbon black (Super P)/PVdF binder = 92/4/4 (w/w/w) in NMP) onto aluminum foils and followed by vacuum drying at 120 $^{\circ}$C. Coin (2032)-type half cells were assembled by sandwiching a polyethylene separator (thickness = 20 μm) between the composite cathode and a lithium metal foil anode, and then activated by filling the liquid electrolyte (1 M LiPF$_6$ in ethylene carbonate (EC)/dimethyl carbonate (DMC) = 1/1 (v/v)). The cell performance was investigated using a cycle tester (PNE Solution) under various charge/discharge conditions.

2.3. Results and discussion

2.3.1. Fabrication and characterization of OLO@MC

The PIL (denoted as "PVIm[DS]") synthesized herein consists of poly(1-vinyl-3-ethylimidazolium) cations and dodecyl sulfate counter anions, whose molecular structures are rationally designed to enable the multiple functions described below. PVIm serves as a precursor for the carbon shell featuring continuous/conformal nanothickness surface coverage, while the DS acts as a porogen (i.e., a pore-generating agent) for realizing the mesoporous structure in the carbon shell. The nitrogen (N) of PVIm and the sulfur (S) of DS provide a dual (N and S)-doping source. The embedding of SWCNTs into the dual-doped mesoporous carbon (MC) shell further increases the electronic conductivity. During the preparation of the PVIm[DS]/SWCNT coating solution, PVIm[DS] allows homogeneous dispersion of the SWCNTs even in the absence of traditional surfactants, revealing its additional function as a polymeric dispersant. Benefiting from the structural/physicochemical uniqueness mentioned above, the SMC shell exhibits unprecedented synergistic effects as an ion/electron-conductive nanoshield (i.e., mitigating interfacial side reactions between cathode materials and liquid electrolytes while facilitating redox reaction kinetics), thereby enabling significant improvements in the electrochemical performance and thermal stability of the cathode materials.

First, the PVIm[Br] was synthesized using traditional radical polymerization[49-50]. Its reaction scheme is presented in Fig. 2A. The ^{1}H NMR spectrum (Fig. 3)[50-51] verified the successful synthesis of PVIm[Br]. Meanwhile, PVIm[DS] was obtained by adding sodium dodecyl sulfate (SDS) to the PVIm[Br] aqueous solution. The initially transparent yellowish solution turned abruptly into an opaque/white suspension (photographs in Fig. 2A) due to the difference in the hydrophilicity of the two PILs[48-50]. DS$^-$ anions are more hydrophobic than Br$^-$ anions, and thus cause the resulting PVIm[DS] to be less soluble in the aqueous solution, leading to the precipitation of PVIm[DS]. Details on the synthesis of these PILs were described in the experimental section. The anion exchange reaction (from Br$^-$ to DS$^-$ anions) was further confirmed by FT-IR spectra (Fig. 4). In addition to the characteristic peaks (1548, 1446, and 1158 cm^{-1}) of imidazolium rings[52], a new FT-IR peak (1209 cm^{-1}) assigned to skeletal vibration of the S−O bridge (in SO$_4^-$ groups)[53] appeared in PVIm[DS], demonstrating that the Br$^-$ anions were successfully exchanged with DS$^-$ anions.

Prior to in-depth characterization of the MC-coated (or SMC-coated) OLO powders, a supplementary study was undertaken with a PVIm[DS]-derived model carbon film (carbonized at 600 ˚C for 2 h in an Ar atmosphere) to better understand the dual-doped mesoporous carbon structure of the MC shell. It is known that the chemical structure of the PIL (or IL) affects the doping content, atomic composition, graphitization, and specific surface area of the resultant carbonized substances[45, 54]. The XPS analysis of the model carbon film showed characteristic N 1s and S 2p peaks, verifying dual (N and S)-doping. The N 1s XPS peaks (shown in Fig. 2B) of the model carbon film were

deconvoluted into three peaks[55]: 398.4 (pyridinic N), 400.2 (pyridonic and/or pyrrolic N), and 401.1 eV (quaternary N), whereas PVIm[DS] itself (i.e., before carbonization) showed an XPS peak at 401.4 eV, which corresponds to imidazolium cations[56-57]. This result manifests the structural re-ordering of the PIL cation backbone during the carbonization. N-doping of carbons is believed to increase electrical conductivity and facilitate diffusion of lithium ions (through C=N bond edges and defects of graphitic carbons)[58-59]. In addition to N-doping, S-doping into the model carbon film was detected through the characteristic XPS peaks corresponding to sulfide groups (C–S–C, at 163.8 eV) and oxidized sulfur groups (C–SO$_x$–C, at 169.0 eV)[60] (Fig. 5). These XPS results confirm the dual (N and S)-doping in the model carbon film.

The Raman spectra of the model carbon film were analyzed and compared with those of PVIm[DS] itself (i.e., before carbonization, Figure 2C). The characteristic peaks[61] assigned to the G-band (1597 cm^{-1}, graphite-like in-plane mode) and D-band (1352 cm^{-1}, disorder mode) were observed at the model carbon film. Moreover, the higher intensity of the G-band with respect to the D-band (I_D/I_G = 0.84) reveals the formation of a highly graphitized structure. The HRTEM images of the model carbon film verified that the graphitic layers were successfully formed (Fig. 2D). Furthermore, the intensity profiles (Fig. 6) showed that the graphitic d spacing (0.397 nm) is similar to the theoretical spacing (0.335 nm) between graphite sheets. In addition, a number of mesopores were formed in the model carbon film. This HRTEM result, along with the aforementioned XPS and Raman spectra, demonstrates that the carbonization of PVIm[DS] leads to the successful formation of dual (N and S)-doped mesoporous graphitic carbon.
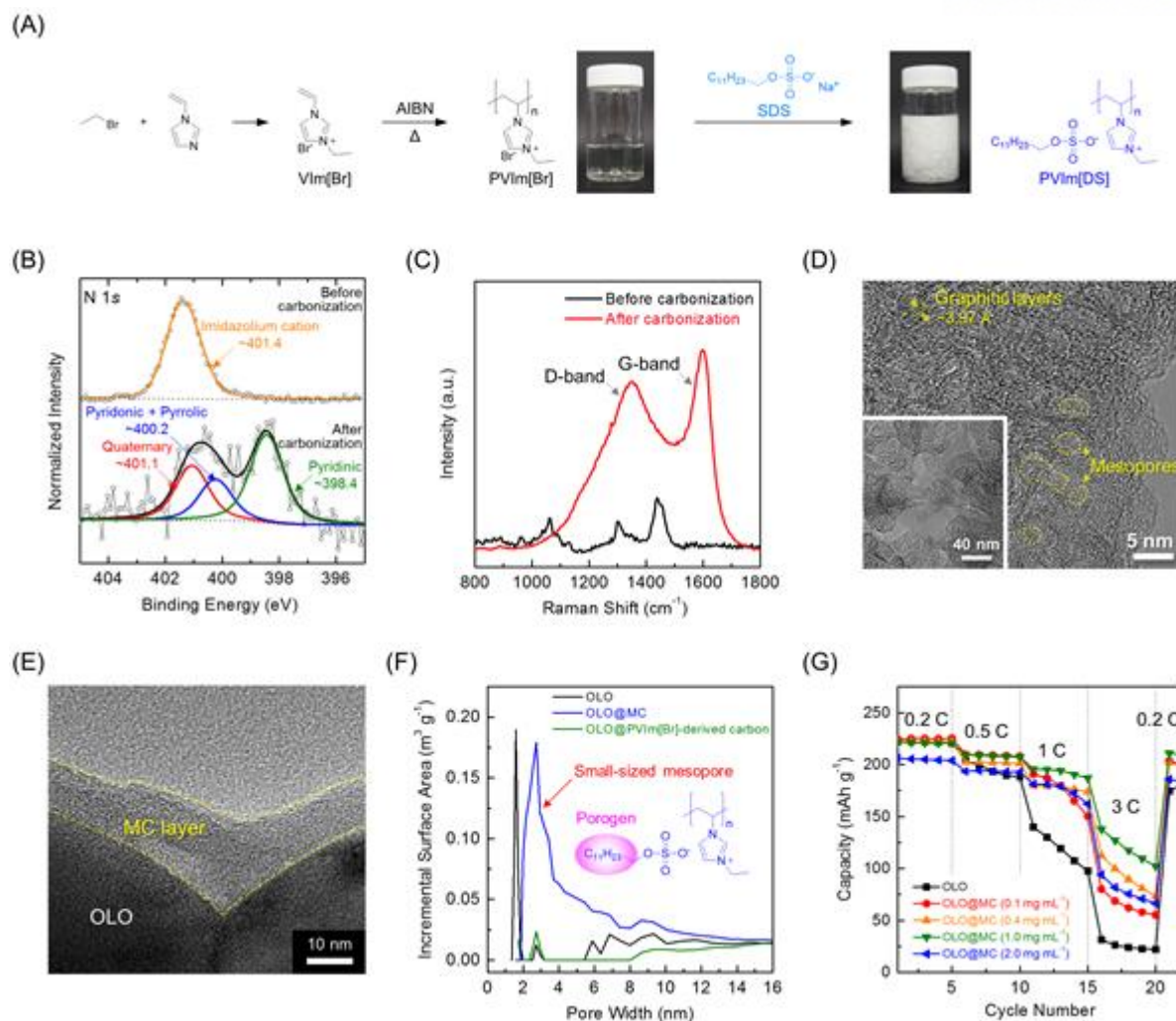
Figure 2. Structural and electrochemical characterizations of OLO@MC. (A) Synthetic scheme of PVIm[Br] and PVIm[DS], along with photographs showing their solution state. (B) XPS N 1s spectra of the PVIm[DS]-derived model carbon film before/after carbonization. (C) Raman spectra of PVIm[DS]-derived model carbon film before/after carbonization. (D) HRTEM images of the PVIm[DS]-derived model carbon film (inset shows a low-magnification view). The yellow arrow indicates the formation of graphitic carbon layers. (E) TEM image of OLO@MC particles. (F) Pore size distributions of pristine OLO, OLO@MC, and OLO@PVIm[Br]-derived carbon. (G) Effect of OLO@MC on discharge rate capability of cells (OLO@MC cathode/polyethylene separator/Li metal anode) as a function of initial concentration (varying from 0.1 to 2.0 mg mL^{-1}) of the PVIm[DS] coating solution.

Figure 3. ^{1}H-NMR spectrum of PVIm[Br].

Figure 4. FT-IR spectra of PVIm[Br] and PVIm[DS], along with their chemical structures.

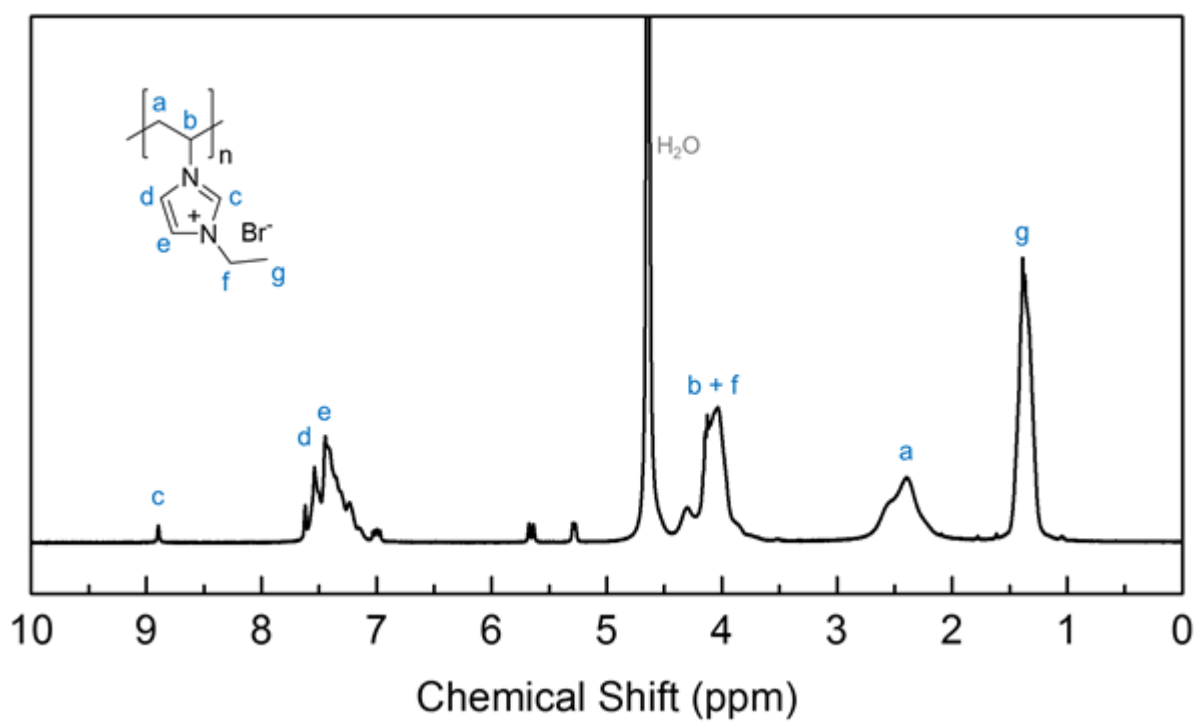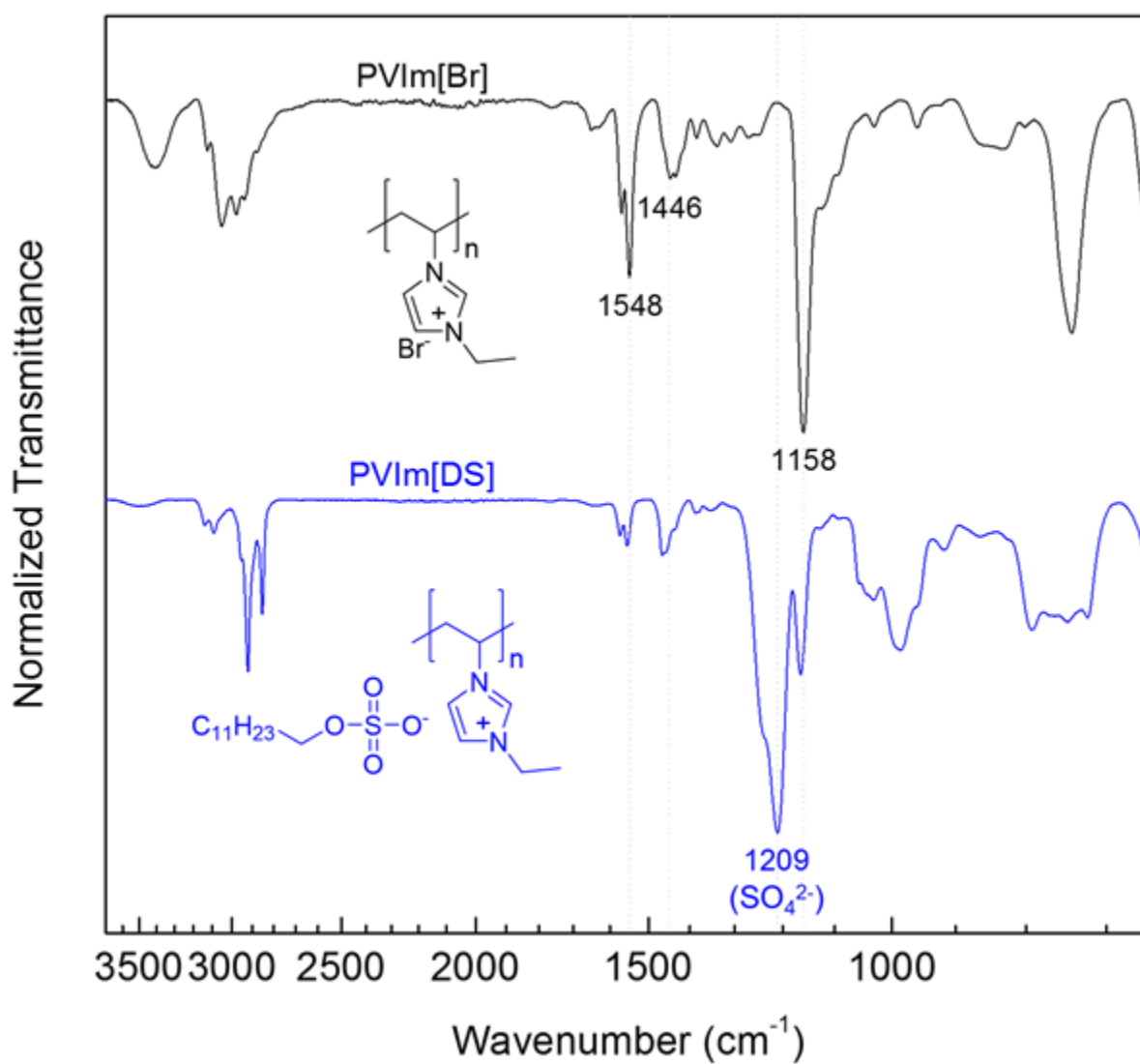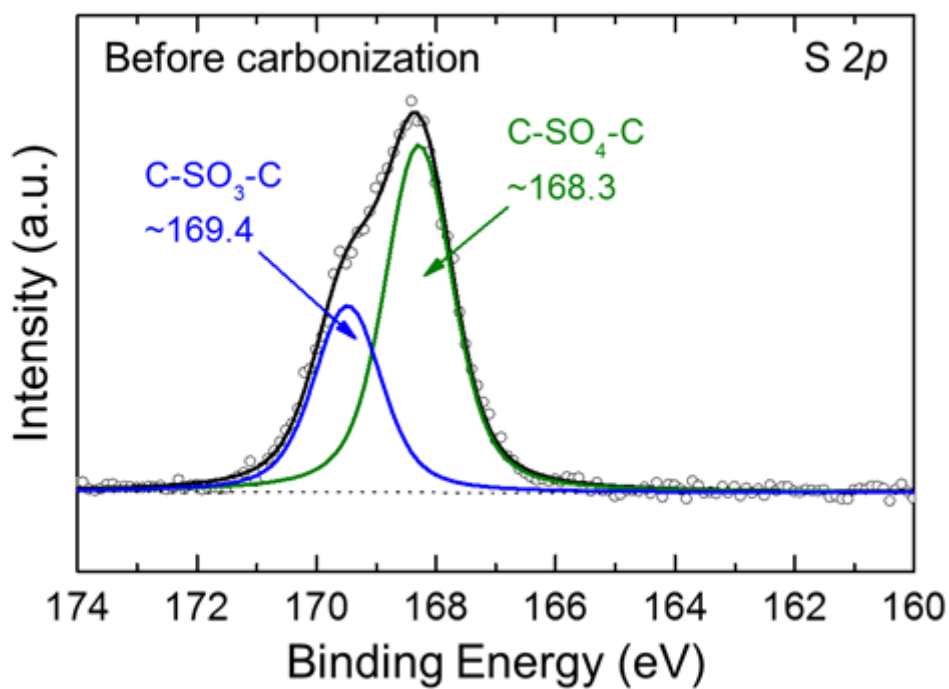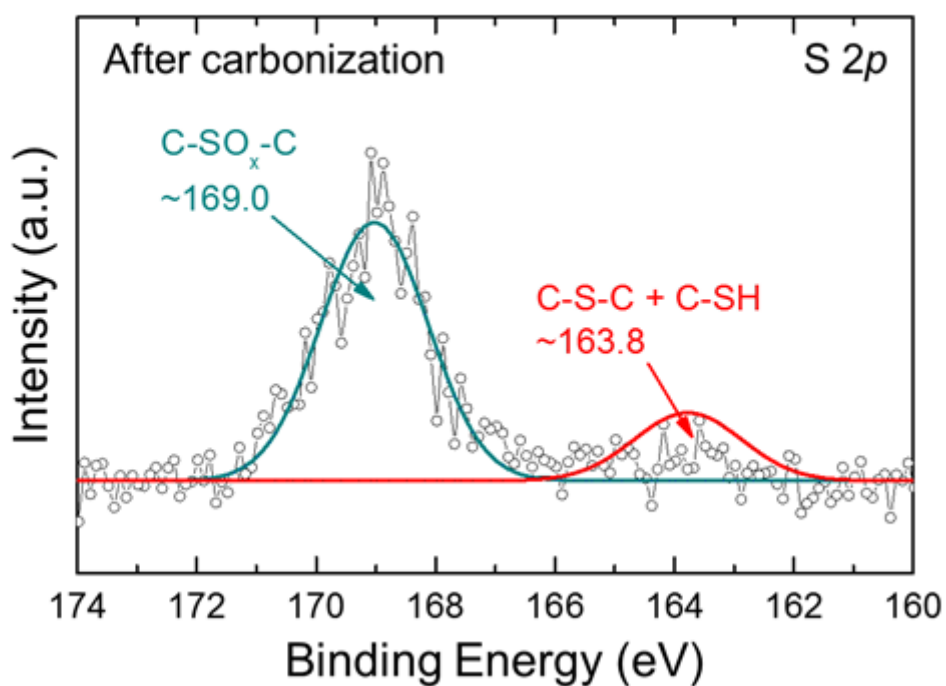**Figure 5.** XPS S 2*p* spectra of PVIm[DS]: (A) Before carbonization. (B) After carbonization (at 600 ˚C for 2 h in Ar atmosphere).
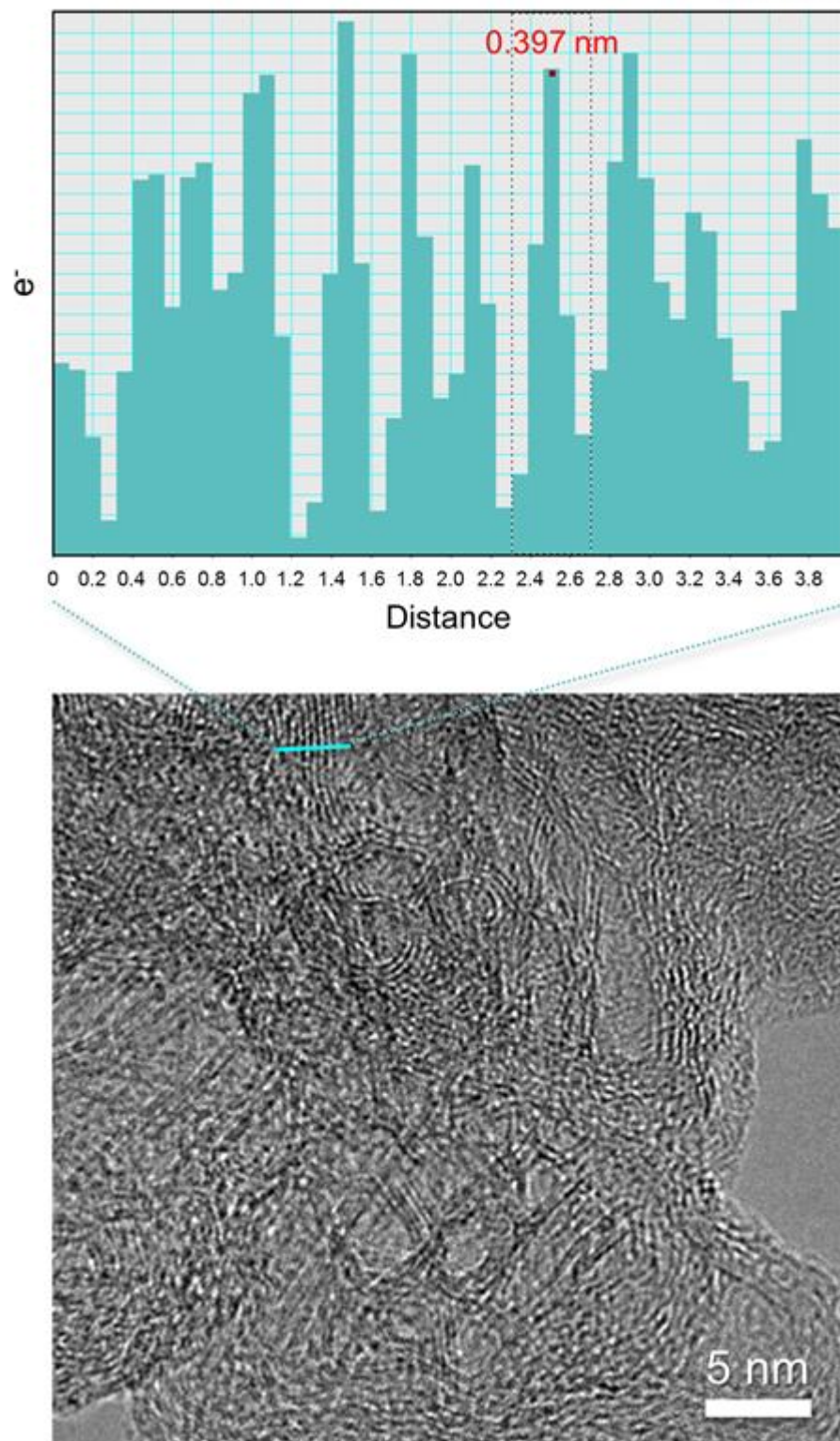
Figure 6. (Bottom) HRTEM image of PVIm[DS]-derived model carbon film and (Top) its intensity profile.

Based on this structural understanding of dual (N and S)-doped mesoporous graphitic carbon, MC shell-coated OLO (denoted as "OLO@MC") particles were characterized and their application to LIB cathodes was explored. The OLO@MC particles were obtained by dispersing OLO particles in the PVIm[DS] coating solution (concentration = 1.0 mg mL^{-1}), and then, undergoing carbonization at 600 ˚C for 2 h. SEM images showed no significant difference in morphology between the OLO and OLO@MC particles (Fig. 7), indicating that continuous and extremely thin MC shells were formed on the OLO particles. In addition, the transmission electron microscopy (TEM) image of OLO@MC showed that OLO particles were coated with nanothick (<20 nm) MC shells (Fig. 2E).

The mesoporous structure of the MC shells formed on the OLO particles was further characterized using N_2 adsorption-desorption isotherms (Fig. 2F and Fig. 8). The specific surface area of OLO@MC (4.978 m^2 g^{-1}) was larger than that of pristine OLO (3.605 m^2 g^{-1}). Notably, the pore size distribution, which was obtained from the N_2 adsorption isotherm by using the density functional theory (DFT) method[62], clearly showed the presence of small-sized mesopores in the OLO@MC particles. As a control sample, PVIm[Br]-derived carbon shells were formed on OLO particles. Intriguingly, no appreciable levels of mesopores were detected in the control sample (Fig. 2F). These results demonstrate that the DS$^-$ anions of PVIm[DS] play a viable role as a porogen in the realization of mesoporous MC shells. In particular, the long alkyl chains ($C_{12}H_{25}$) of the DS$^-$ anions are responsible for mesopore generation after carbonization. In comparison, Br$^-$ anions do not contain such alkyl chains and are thus ineffective as porogens. These results underline the importance of the molecular design of PIL anions for generating mesoporous structures.

The dual-doped mesoporous MC shells described above are expected to simultaneously facilitate ion (via the mesopores) and electron (through the dual-doped carbon) transport toward OLO materials while mitigating direct contact with the bulk liquid electrolyte. The effect of the MC shells on the electrochemical performance of OLO@MC was investigated using a coin-type cell (OLO@MC cathode/polyethylene separator/Li metal anode). The composition ratio and areal mass loading of the OLO@MC cathode were OLO@MC/carbon black/polyvinylidene fluoride (PVdF) binder = 92/4/4 (w/w/w) and 7 mg cm^{-2}, respectively. To elucidate the effect of the PVIm[DS] content on the cell performance, the initial concentration of the PVIm[DS] coating solution was varied from 0.1 to 2.0 mg mL^{-1}. The cells were charged at a constant current density of 0.2 C (0.34 mA cm^{-2}) and discharged at current densities varying from 0.2 to 3.0 C in a voltage range of 2.0–4.7 V. All of the OLO@MC cathodes examined herein showed higher discharge capacities than the pristine OLO cathode over a wide range of discharge-current densities (Figure 2G), demonstrating that MC shells improve the discharge rate capability due to their facile ion/electron conduction. The discharge rate capability of OLO@MC improved with increasing concentration of PVIm[DS] coating solution. The higher PVIm[DS] concentration led to an increase in the electrical conductivity of the resulting OLO@MC cathodes (Fig. 9), which could reasonably account for the enhanced discharge rate capability. Notably,

the discharge rate capability of the 1.0 mg mL^{-1} PVIm[DS] coating solution was the highest among all concentrations tested herein. For the 2.0 mg mL^{-1} PVIm[DS] coating solution, the electrical conductivity appeared similar to that of the 1.0 mg mL^{-1} PVIm[DS] coating solution. On the other hand, the considerably more MC shell was generated at the 2.0 mg mL^{-1} PVIm[DS] coating solution (Fig. 10). Furthermore, the thick MC shells were inhomogeneously deposited on OLO particles (Fig. 11), which may not be favorable for electrolyte wettability and ionic migration through the MC shell. As a result, the relatively sluggish ionic transport through thick/irregularly deposited MC shells may give rise to the inferior discharge rate capability compared to the result for the 1.0 mg mL^{-1} PVIm[DS] coating solution. Meanwhile, the larger amount of MC shells in the OLO@MC particles (shown in Fig. 10), along with the relatively poor electrolyte wettability, may negatively affect the initial gravimetric specific capacity.
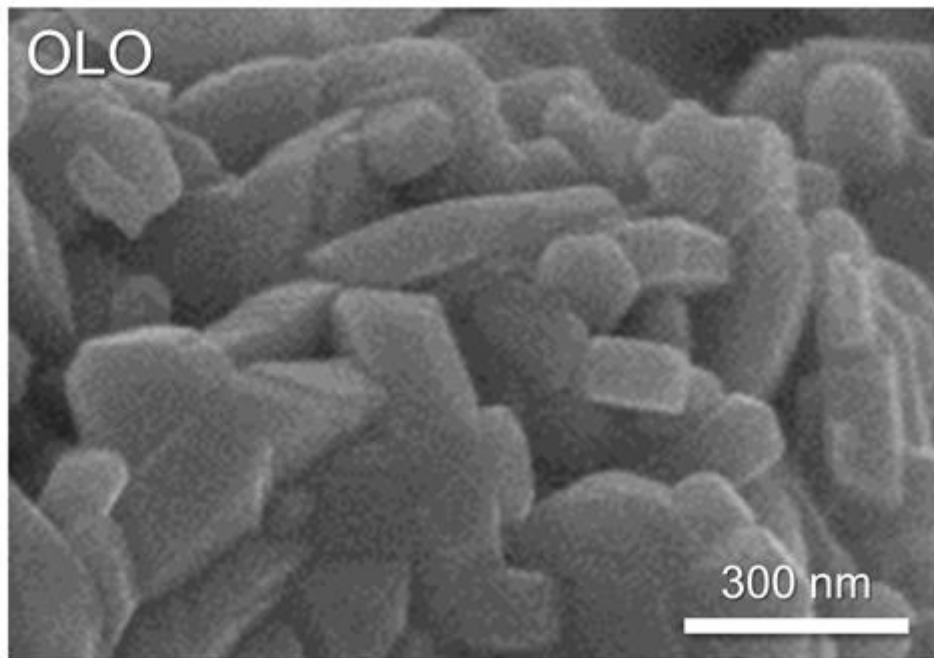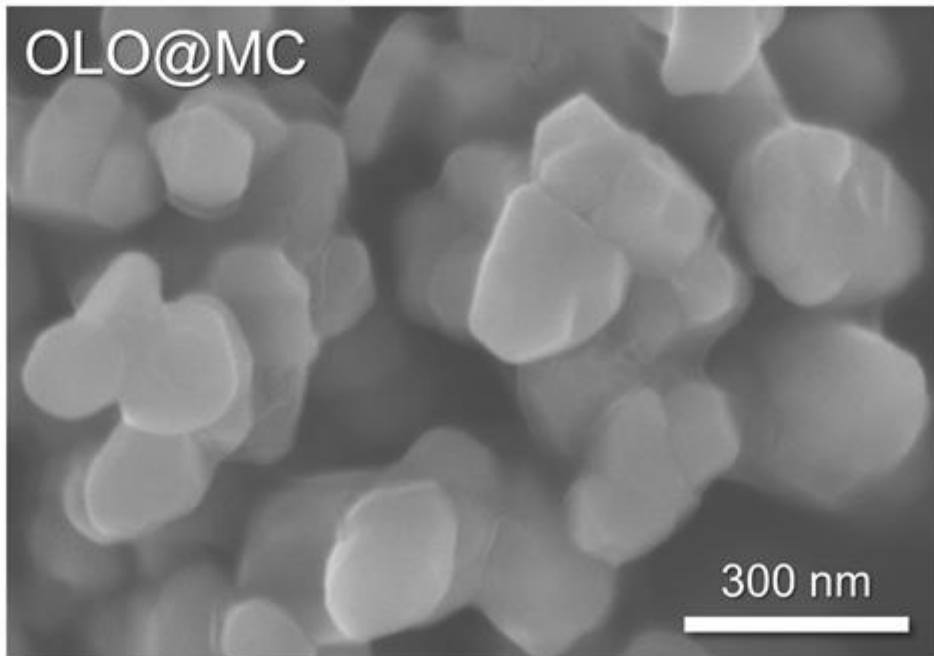
Figure 7. SEM images of (A) pristine OLO and (B) OLO@MC powders.
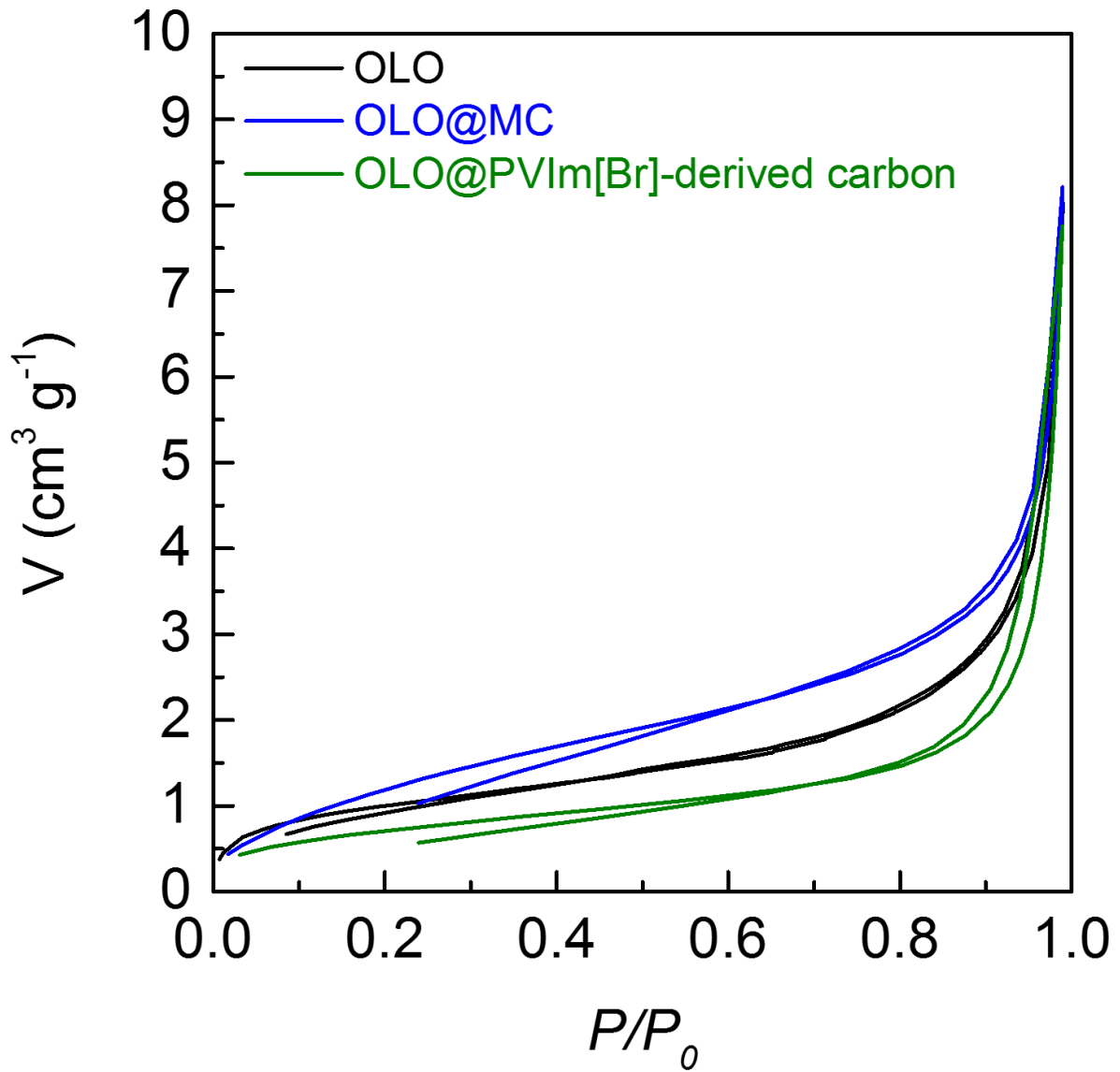
Figure 8. N$_2$ adsorption-desorption isotherms of the pristine OLO, OLO@MC, and OLO@PVIm[Br]-derived carbon.
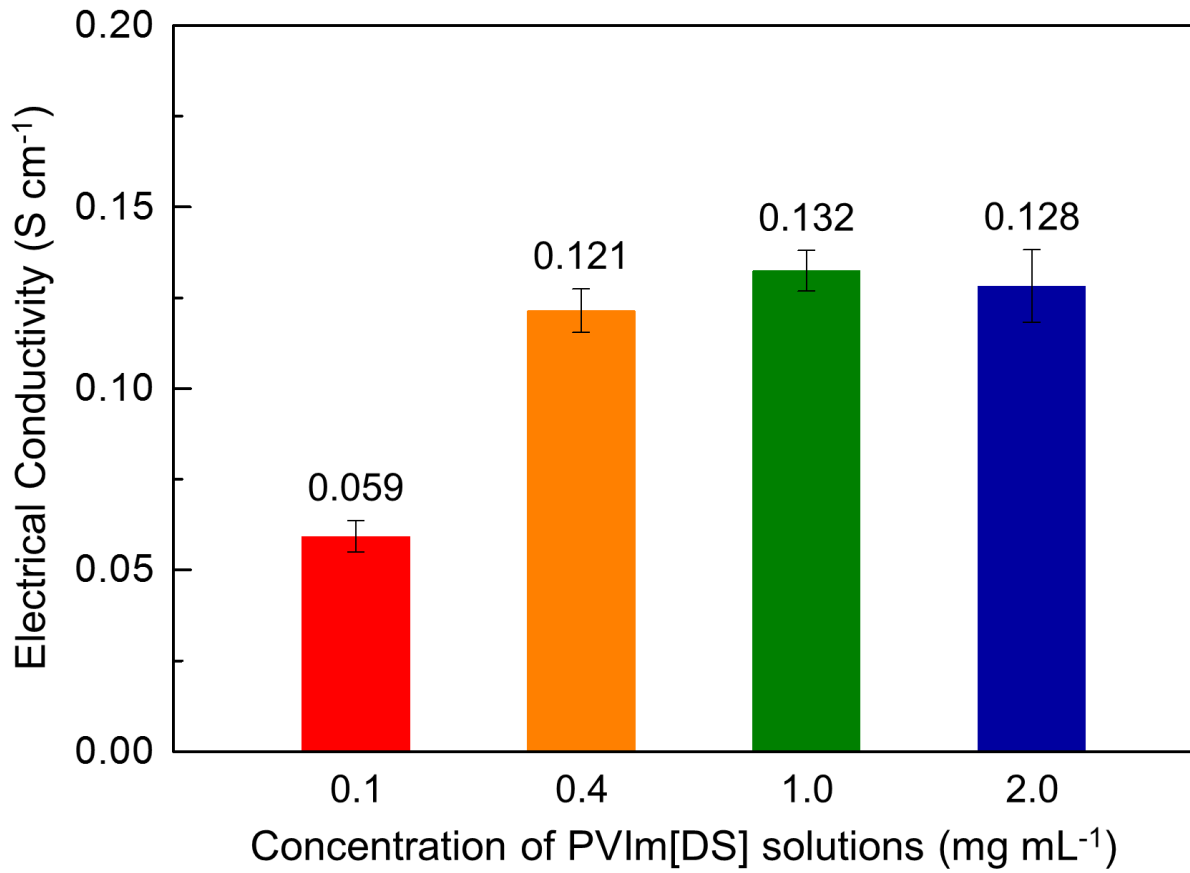
Figure 9. Electrical conductivity of the OLO@MC cathodes as a function of initial concentration (varying from 0.1 to 2.0 mg mL^{-1}) of the PVIm[DS] coating solution.
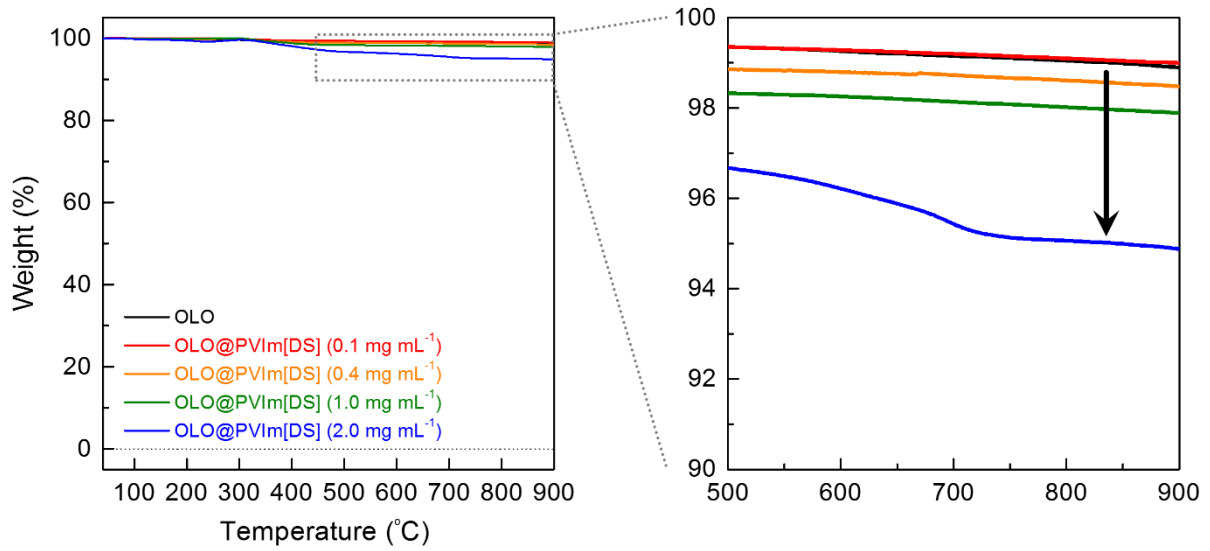
Figure 10. TGA profiles of OLO@MC as a function of initial concentration (varying from 0.1 to 2.0 mg mL^{-1}) of the PVIm[DS] coating solution.
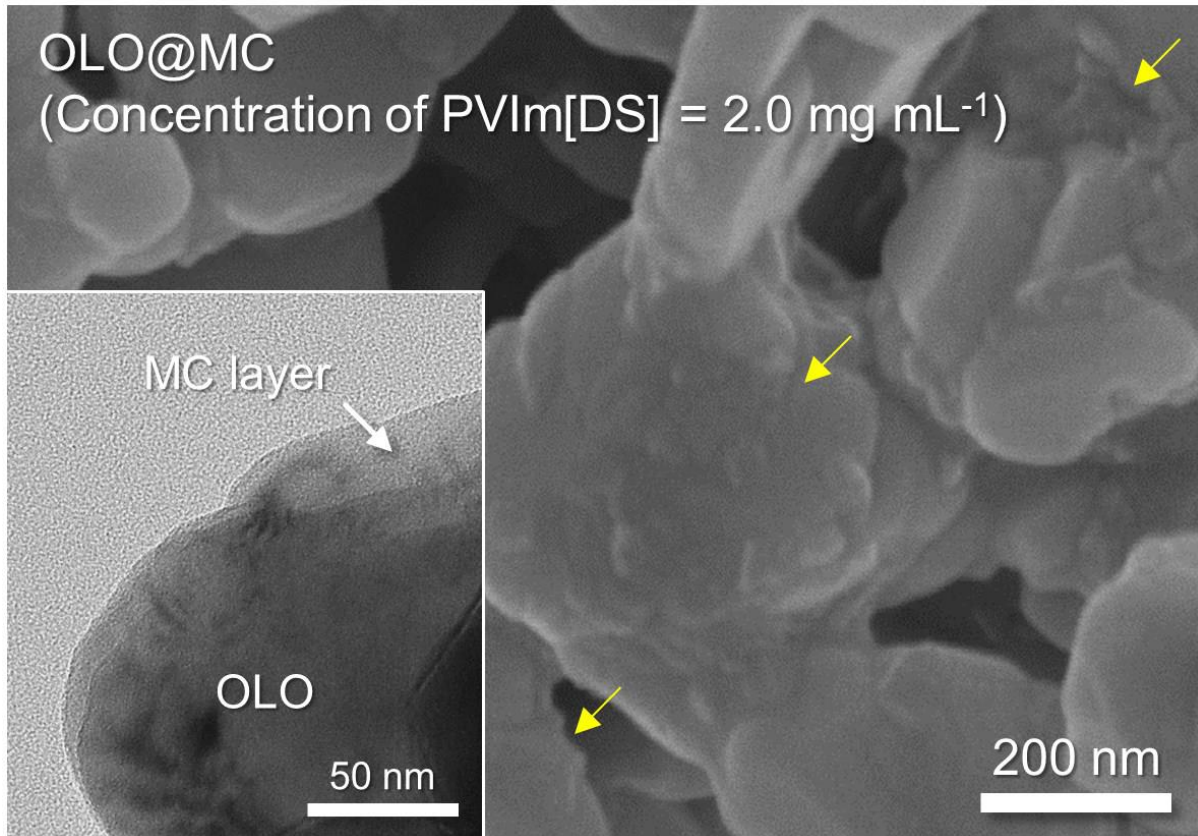
Figure 11. SEM and HRTEM (inset) images of OLO@MC prepared from PVIm[DS] coating solution with initial concentration of 2.0 mg mL^{-1}. Yellow arrows indicate the thick and irregularly-deposited MC shell on the OLO surface.

2.3.2. Fabrication and characterization of OLO@SMC

In an attempt to further increase the electrical conductivity of MC shells, 2 wt% (relative to the PVIm[DS] content) SWCNTs were added to the PVIm[DS] coating solution, eventually yielding SWCNT-embedded MC (denoted as "SMC") shells. A prerequisite for the realization of SMC shells is the good dispersion of SWCNTs in the PVIm[DS] coating solution. The PVIm[DS] coating solution allowed a better dispersion state of SWCNTs than both the PVIm[Br] coating solution and the SDS surfactant-added N,N-dimethylacetamide (DMAc) solvent (Fig. 2A). The dispersion states of SWCNTs in the mixed solutions were further analyzed using vis-NIR spectroscopy, for which the samples were centrifuged (10,000 g) and the supernatant solutions were collected exclusively for this characterization. The SWCNT/PVIm[DS] coating solution exhibited a substantially higher absorbance than the other coating solutions (Figure 12B), verifying the good dispersion state of SWCNTs. These results demonstrate the synergistic effect of $PVIm^+$ cations and DS^- anions on the SWCNT dispersion, underscoring the important contribution of PVIm[DS] as a polymeric dispersant for SWCNTs. This advantageous function of PVIm[DS] is illustrated schematically in Figure 12A.

As a next step, the OLO cathode materials were mixed with the above-prepared SWCNT/PVIm[DS] coating solution. Fig. 12C shows that the highly interconnected SWCNT networks were uniformly distributed over the OLO particles (inset shows pristine OLO). After carbonization at 600 ˚C for 2 h, the SWCNT/PVIm[DS] coating layer transformed into SMC shells on the OLO particles (i.e., OLO@SMC). Fig. 12D shows that the SWCNT networks were formed on the OLO particles with being embedded into the conformal/continuous MC shell. No structural disruption of the OLO particle was proved after the introduction of SMC shells (Figure 13). The highly reticulated SWCNTs embedded in the MC shells act as electron highways that spatially connect the OLO particles in addition to offering additional electron-conductive routes to the MC shell, eventually boosting the electron transport of the resultant OLO@SMC (electrical conductivity [S cm^{-1}] = 0.58 for OLO@SMC vs 0.06 for pristine OLO vs 0.13 for OLO@MC). These well-developed electron pathways, in combination with ion migration via mesopores of the MC shells, are expected to improve the electrochemical performance of the OLO@SMC particles. Such interesting ion/electron transport phenomena are illustrated schematically in Fig. 12E.

Figure 12. PVIm[DS]-assisted dispersion of SWCNTs and structural characterization of OLO@SMC. (A) (Top) Photographs of SWCNT/DMAc suspensions incorporating PVIm[Br], SDS, and PVIm[DS]. (Bottom) Schematic illustration depicting the advantageous effect of PVIm[DS] on the SWCNT dispersion (i.e., synergistic effect of PVIm$^+$ cations and DS$^-$ anions). (B) vis-NIR absorption spectra of SWCNT/DMAc suspension incorporating PVIm[Br], SDS, and PVIm[DS], wherein the samples were

subjected to centrifugation (10,000 g) and the supernatant solutions were collected exclusively for this characterization. (C) SEM images of OLO powders coated with SWCNT/PVIm[DS] coating solution. (D) SEM (left) and HRTEM (right) images of OLO@SMC. The SWCNTs embedded in the MC shells were marked with yellow circles. (E) Conceptual illustration depicting the structural uniqueness of SMC shells and their contribution to the ion/electron transport phenomena.

Figure 13. XRD patterns of the pristine OLO and OLO@SMC powders.

We investigated the effect of OLO@SMC on cell performance using a coin-type cell (OLO@SMC cathode/polyethylene separator/Li metal anode). The composition ratio and areal mass loading of the OLO@SMC cathode were OLO@SMC/carbon black/PVdF binder = 92/4/4 (w/w/w) and 7 mg cm^{-2}, respectively. Figure 14A shows the discharge rate capability of cells, wherein the cells were charged at a constant current density of 0.2 C (0.34 mA cm^{-2}) and discharged at various current densities ranging from 0.2 to 5.0 C. The discharge rate capability of OLO@SMC was superior to those of both pristine OLO and OLO@MC, which became more pronounced at higher discharge current densities. Such an improvement in the discharge rate capability of OLO@SMC is attributed to the presence of dual-doped mesoporous carbon and also to the additional electron pathways created by the SWCNT networks. To further verify the faster discharge rate perfor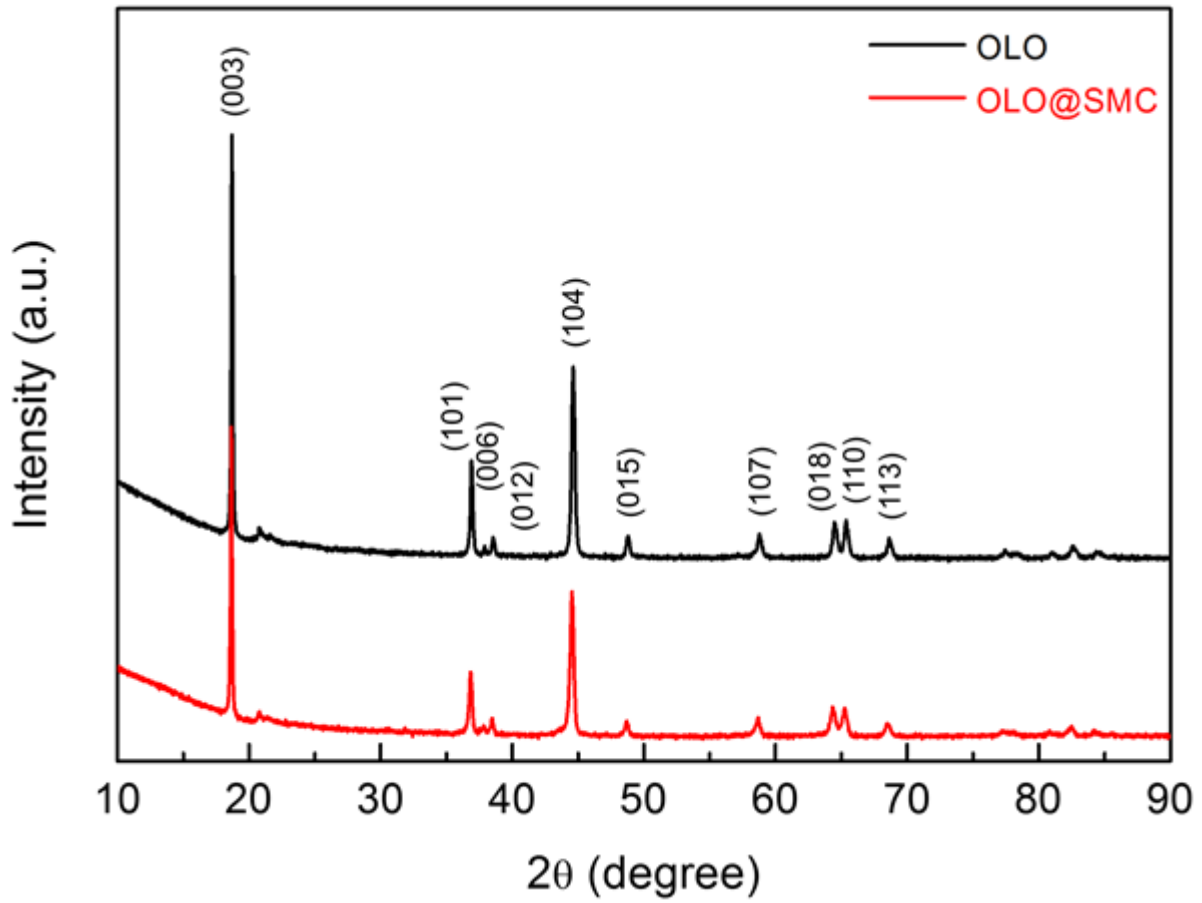mance of OLO@SMC, galvanostatic intermittent titration technique (GITT) analysis[63] was conducted. Upon repeated current stimuli (at current density = 0.5 C, interruption time between each pulse = 60 min) during the charge/discharge reaction, the OLO@SMC effectively alleviated the rise in cell polarization compared with pristine OLO (Figure 14B). The internal cell resistances of OLO@SMC were compared with those of pristine OLO as a function of state of charge (SOC) and depth of discharge (DOD), confirming the advantageous effect of the SMC shell on the faster redox reaction of OLO cathode materials.

The cycling performance of OLO@SMC was also examined, where the cells were cycled at charge/discharge current density of 3.0 C/3.0 C under voltage range of 2.0–4.7 V. Here, to clarify the beneficial effect of SMC shells, the areal mass loading of the cathodes was set to 14 mg cm^{-2}, which is significantly higher than previously reported results (Table 1). Figure 14C shows that OLO@SMC retains higher capacity (79.0% after 50 cycles) than both pristine OLO (41.3%) and OLO@MC (60.8%). Moreover, the suppression of cell polarization with cycling was observed in the charge/discharge profiles (Figure 15).

To better understand the beneficial effect of OLO@SMC on the cycling performance, a postmortem analysis of the cells was conducted after the cycling test. The surface of the OLO@SMC cathode was relatively clean (Fig. 14D), whereas the control OLO cathode was covered with a substantial amount of randomly aggregated byproducts (see inset of Fig. 14D). The byproducts that formed on the cathodes were further analyzed using XPS and time-of-flight secondary-ion-mass spectroscopy (TOF-SIMS). The XPS F 1*s* spectra (Figure 14E) revealed LiF formation on the cathodes, which is one of unwanted byproducts generated by hydrofluoric acid (HF, generated from residual water-induced decomposition of LiPF$_6$-incorporating electrolytes)-triggered interfacial side reactions[27, 64-65]. An intriguing finding is that the peak intensity of LiF was lower at the OLO@SMC cathode, indicating that SMC shells effectively suppressed the interfacial side reactions between OLO and liquid electrolyte during cycling. This contribution of the SMC shells to the LiF suppression was confirmed by TOF-SIMS images (Figure 14F). LiF was sparsely dispersed over a wide area of the OLO@SMC cathode and its absolute amount was less than that for the control OLO cathode.

Furthermore, the HF in the liquid electrolyte is known to attack OLO cathode materials, thereby accelerating dissolution of heavy metal ions (e.g., Mn^{2+}) from the OLO cathode materials[30, 64, 66]. The dissolved Mn^{2+} ions migrate toward lithium anodes and are reduced to metallic Mn on the anode surface. The inductively coupled plasma-optical emission spectrometry (ICP-OES, Figure 14G) results showed that a considerable amount of metallic Mn (180 ppm) was deposited on the lithium anode assembled with the control OLO. In comparison, the OLO@SMC remarkably suppressed the Mn deposition to 4.4 ppm, demonstrating the beneficial contribution of the SMC shell as a protective layer that mitigates the direct exposure of OLO to the HF-containing liquid electrolyte. The metallic Mn deposited on the lithium anode, along with the structural contamination of the OLO cathode materials mentioned above, is believed to provoke serious capacity fading during cycling[29, 66]. These postmortem results on the electrode surface underscore the advantageous effects of the SMC shells as exceptional ion/electron-conductive nanoshields.

Delithiated cathode materials tend to generate interfacial exothermic reactions upon exposure to liquid electrolytes[40, 64], which becomes more serious with high-capacity/high-voltage cathode materials. The DSC thermograms (Figure 14H) showed that OLO@SMC (ΔH_{exo} = 589 J g^{-1}, T_{peak} = 276 ˚C) noticeably improved the thermal stability compared to the control OLO (ΔH_{exo} = 1089 J g^{-1}, T_{peak} = 265 ˚C). This result demonstrates that the conformal/continuous SMC shell effectively prevents the exposure of OLO to bulk liquid electrolyte, thereby alleviating the unwanted exothermic reaction at the cathode–electrolyte interface.

Figure 14. Effect of OLO@SMC on the electrochemical performance of coin (2032-type) cells. (A) Discharge rate capability of pristine OLO, OLO@MC, and OLO@SMC, wherein the cells were charged at a constant current density of 0.2 C (0.34 mA cm^{-2}) and discharged at various current densities ranging from 0.2 to 5.0 C. (B) (Left) GITT profiles of the cells assembled with pristine OLO and OLO@SMC cathodes. (Right) Change in internal cell resistances as a function of state of charge (SOC) and depth of discharge (DOD). (C) Comparison of cycling performance (at charge/discharge current density = 3.0 C/3.0 C under voltage range of of 2.0–4.7 V) between pristine OLO, OLO@MC, and OLO@SMC. (D)–(G) Analysis of cells (OLO vs OLO@SMC) after cycling test (50 cycles): (D) SEM image of OLO@SMC cathode. The inset shows the morphology of the OLO cathode. (E) XPS F 1*s* spectra of the OLO and OLO@SMC cathodes. (F) TOF-SIMS images of the LiF byproducts formed on the OLO and OLO@SMC cathodes. (G) ICP-OES results showing the amount of metallic Mn deposited on the Li metal anodes assembled with the OLO and OLO@SMC cathodes. (H) DSC thermograms showing interfacial exothermic reaction between delithiated (charged to 4.7 V) OLO cathodes and liquid electrolyte.

Table 1. Comparison of composite ratio and areal mass loading used in this study with previously reported results.

| Publication /Chemical structure of OLO	Composite ratio (%)			Mass Loading (mg cm^{-2})
	Active material	Conductive agent	Binder	
This work /**$0.49Li_2MnO_3 \cdot 0.51LiNi_{0.37}Co_{0.24}Mn_{0.39}O_2$**	**92**	**4**	**4**	**~14**
Adv. Mater. **2015**, *27*, 3915. /$Li[Li_{0.2}Mn_{0.568}Ni_{0.2}X_{0.032}]O_2$ (X = Si, Sn, and Mn)	80	10	10	2 - 3
Adv. Energy Mater. **2015**, *5*, 1500274. /$Li_{1.17}Ni_{0.17}Co_{0.17}Mn_{0.5}O_2$($0.4Li_2MnO_3 \cdot 0.6Li Ni_{1/3}Co_{1/3}Mn_{1/3}O_2$)	80	10	10	4.5
Adv. Energy Mater. **2013**, *3*, 1299. /$Li_{1.2}Ni_{0.13}Mn_{0.54}Co_{0.13}O_2$	80	10	10	2.9
Nano Lett. **2014**, *14*, 5965. /hydrazine treated $0.5Li_2MnO_3$-$0.5LiNi_{0.5}Mn_{0.5}O_2$	90	5	5	6.2
J. Mater. Chem. A **2015**, *3*, 17113. /$Li[Li_{0.2}Co_{0.13}Ni_{0.13}Mn_{0.54}]O_2$	80	10	10	2
J. Mater. Chem. A **2015**, *3*, 13933. /$0.5Li_2MnO_3 \cdot 0.5LiNi_{0.5}Co_{0.2}Mn_{0.3}O_2$	85	10	5	3
J. Mater. Chem. A **2015**, *3*, 17627. /$Li(Li_{0.17}Ni_{0.25}Mn_{0.58})O_2$	75	15	10	4.97
ACS Appl. Mater. Interfaces **2015**, *7*, 8319. /$Li_{1.17}Ni_{0.17}Mn_{0.5}Co_{0.17}O_2$	80	10	10	4.97
ACS Appl. Mater. Interfaces **2014**, *6*, 21711. /$Li[Li_{0.2}Fe_{0.1}Ni_{0.15}Mn_{0.55}]O_2$	80	10	10	3
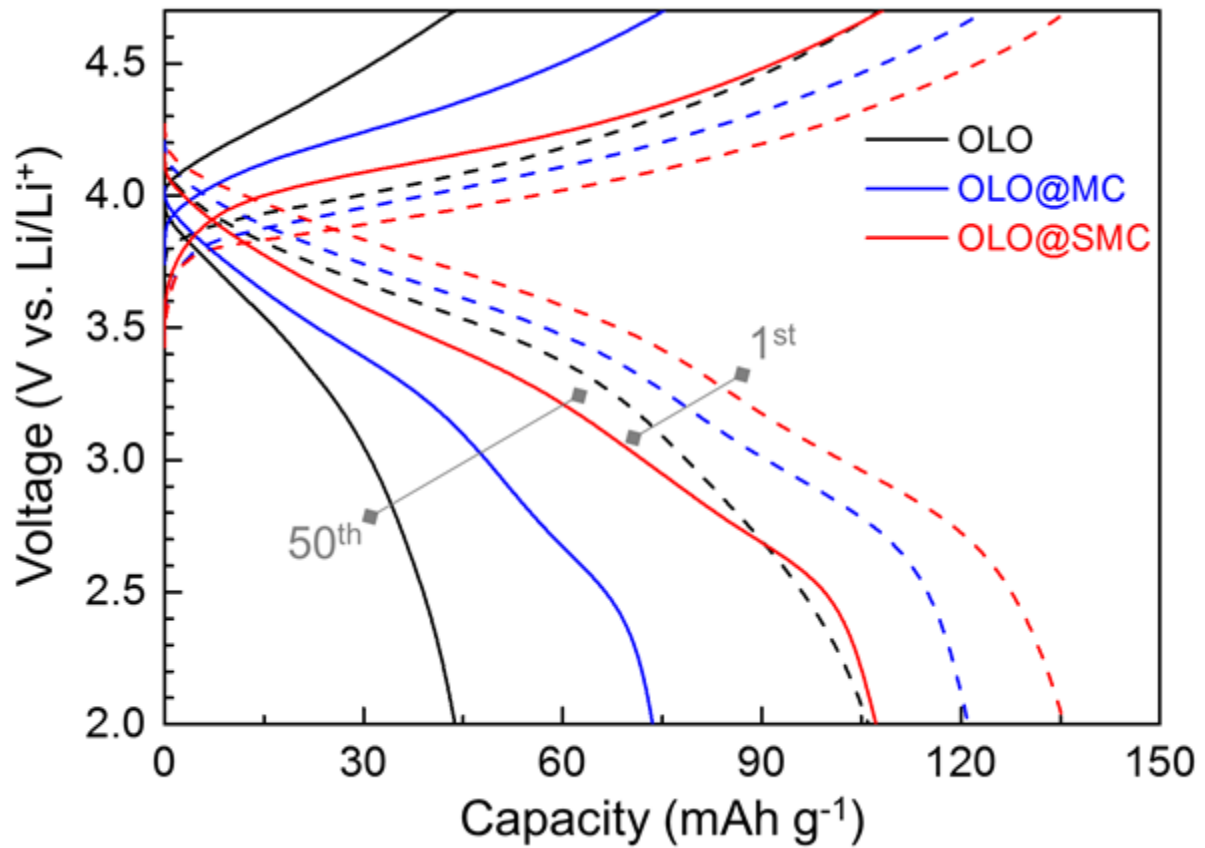
Figure 15. Charge/discharge profiles (for 1st and 50th cycles) of the pristine OLO, OLO@MC, and OLO@SMC cathodes, wherein the cells were cycled at charge/discharge current density = 3.0 C/3.0 C under voltage range of 2.0 – 4.7 V.

2.3.3. The versatility of the SMC shell concept: LNMO@SMC

To explore the versatility of the SMC shell as an electrochemical/thermal protective layer, its application to high-voltage LNMO cathode materials was investigated in addition to the high-capacity OLO cathode materials described above. Figure 16A shows that the conformal/continuous SMC shell was successfully formed on the LNMO surface, which appeared similar to the morphology of the OLO@SMC in overall. Driven by the SMC shell, the LNMO@SMC provided the higher electrical conductivity than the pristine LNMO (Fig. 16B). As a result, over a wide range of discharge current densities (0.2–10.0C) at a fixed charge current density of 0.2C in a voltage range of 3.5–4.95 V, the cell assembled with the LNMO@SMC showed larger discharge capacities compared with pristine LNMO (Fig. 16C)[67]. Fig. 16D presents that the SMC shell allowed the LNMO@SMC to suppress the interfacial exothermic heat ($\Delta H_{exo} = 143$ J g^{-1}) and to shift the exothermic peak temperature to a higher value ($T_{peak} = 304$ °C), as compared with the pristine LNMO ($\Delta H_{exo} = 286$ J g^{-1}, $T_{peak} = 276$ °C). These results demonstrate that the SMC shell can be suggested as an effective and versatile platform technology for the surface modification of cathode materials.
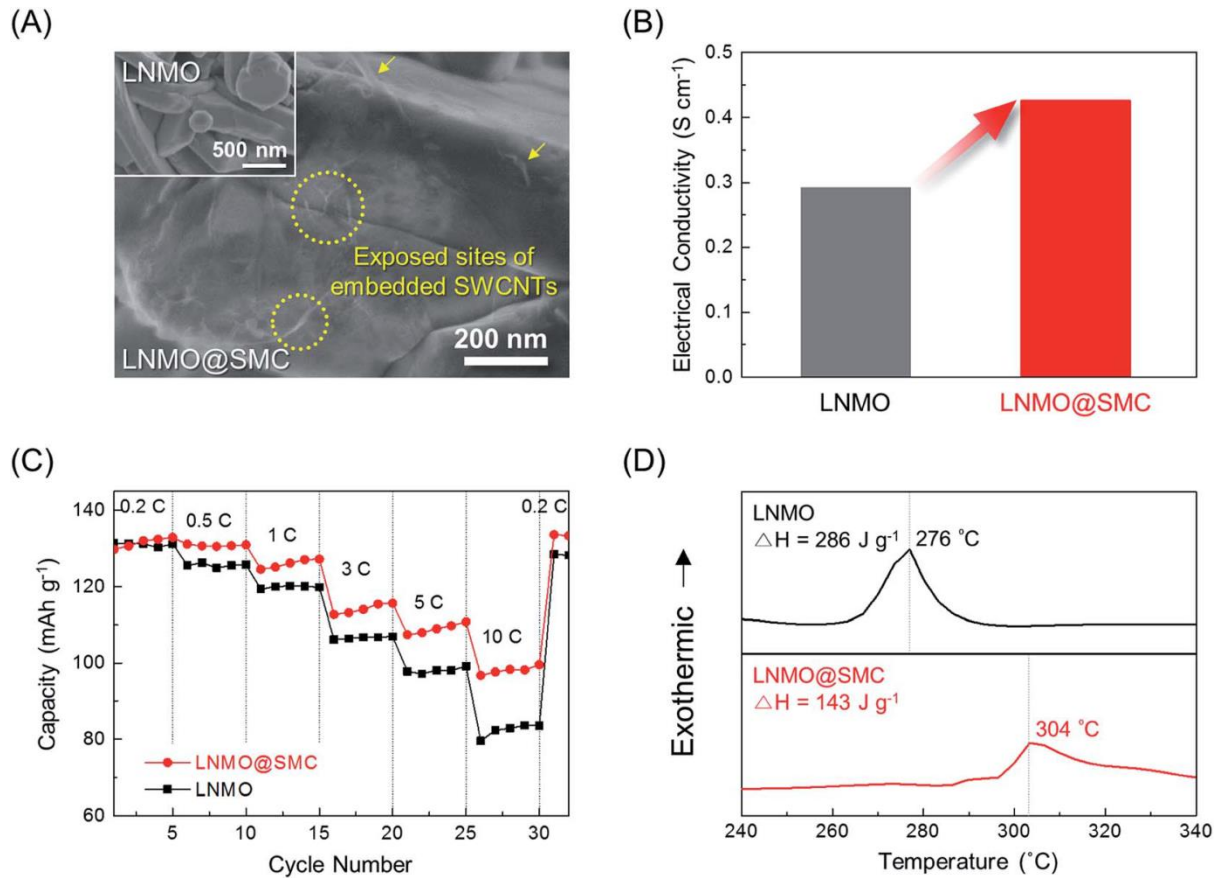
Figure 16. Application of SMC shells to high-voltage LNMO cathode materials. (A) SEM image of LNMO@SMC, wherein the SWCNTs embedded in the MC shells were marked with yellow circles. The inset shows the morphology of pristine LNMO. (B) Electrical conductivity of pristine LNMO and LNMO@SMC. (C) Discharge rate capability of pristine LNMO and LNMO@SMC, wherein the cells were charged at a constant current density of 0.2C and discharged at various current densities ranging from 0.2 to 10.0C. (D) DSC thermograms showing the interfacial exothermic reaction between the delithiated (charged to 4.95 V) LNMO cathodes and liquid electrolyte.

2.4. Conclusion

In summary, we presented a SWCNT-embedded, dual (N and S)-doped mesoporous carbon (SMC) shell as a new concept of molecularly designed, ion/electron-conductive nanoshields to overcome the long-standing challenges (i.e., interfacial problems with liquid electrolytes) facing LIB electrode materials. The mixing of cathode particles with the SWCNT/PVIm[DS] coating solution and the subsequent carbonization led to the formation of SMC shells on the cathode particles. The molecular structure of PVIm[DS] was rationally designed to achieve the following multiple functions: (i) precursor for conformal/continuous nanothickness carbon shells, (ii) dual (N and S)-doping source, (iii) porogen for the mesoporous structure, and (iv) SWCNT dispersant. We comprehensively characterized the SWCNT/PVIm[DS]-derived SMC shells on OLO particles with a particular focus on nanothickness surface coverage, mesopore formation, and electronic conduction. Due to such chemical/structural uniqueness, the SMC shells prevented direct exposure of OLO to the bulk liquid electrolyte while facilitating the redox reaction kinetics of OLO. As a consequence, the OLO@SMC significantly enhanced the cell performance and mitigated the interfacial exothermic reaction between the delithiated OLO and liquid electrolyte, demonstrating the unusual contribution of the SMC shells as ion/electron-conductive nanoshields. The beneficial effects of SMC shells were also observed in the LNMO materials, verifying their versatile applicability. The SMC shell, driven by the molecularly designed PIL and synergistic combination with the SWCNTs, is anticipated to open a new route to an exceptional interfacial control strategy for high-energy density/high-performance electrode materials.

REFERENCES

1.   Armand, M.; Tarascon, J. M., Building better batteries. *Nature* **2008,** *451* (7179), 652-657.

2.   Lee, H.; Yanilmaz, M.; Toprakci, O.; Fu, K.; Zhang, X., A review of recent developments in membrane separators for rechargeable lithium-ion batteries. *Energy Environ. Sci.* **2014,** *7* (12), 3857-3886.

3.   Tarascon, J. M.; Armand, M., Issues and challenges facing rechargeable lithium batteries. *Nature* **2001,** *414* (6861), 359-67.

4.   Zhang, L.; Li, N.; Wu, B.; Xu, H.; Wang, L.; Yang, X. Q.; Wu, F., Sphere-shaped hierarchical cathode with enhanced growth of nanocrystal planes for high-rate and cycling-stable li-ion batteries. *Nano Lett* **2015,** *15* (1), 656-61.

5.   Yan, J.; Liu, X.; Li, B., Recent progress in Li-rich layered oxides as cathode materials for Li-ion batteries. *RSC Adv.* **2014,** *4* (108), 63268-63284.

6.   Hong, Y.-S.; Park, Y. J.; Ryu, K. S.; Chang, S. H.; Kim, M. G., Synthesis and electrochemical properties of nanocrystalline $Li[Ni_xLi(1-2x)/3Mn(2-x)/3]O_2$ prepared by a simple combustion method. *J. Mater. Chem.* **2004,** *14* (9), 1424-1429.

7.   Kim, Y.; Hong, Y.; Kim, M. G.; Cho, J., $Li_{0.93}[Li_{0.21}Co_{0.28}Mn_{0.51}]O_2$ nanoparticles for lithium battery cathode material made by cationic exchange from K-birnessite. *Electrochemistry Communications* **2007,** *9* (5), 1041-1046.

8.   Liu, R.; Duay, J.; Lee, S. B., Heterogeneous nanostructured electrode materials for electrochemical energy storage. *Chem Commun (Camb)* **2011,** *47* (5), 1384-404.

9.   Tang, Z.; Wang, Z.; Li, X.; Peng, W., Preparation and electrochemical properties of Co-doped and none-doped $Li[Li_xMn_{0.65(1-x)}Ni_{0.35(1-x)}]O_2$ cathode materials for lithium battery batteries. *Journal of Power Sources* **2012,** *204*, 187-192.

10.   Tabuchi, M.; Nabeshima, Y.; Takeuchi, T.; Kageyama, H.; Imaizumi, J.; Shibuya, H.; Akimoto, J., Synthesis of high-capacity Ti- and/or Fe-substituted Li_2MnO_3 positive electrode materials with high initial cycle efficiency by application of the carbothermal reduction method. *Journal of Power Sources* **2013,** *221*, 427-434.

11.   Song, B.; Lai, M. O.; Lu, L., Influence of Ru substitution on Li-rich $0.55Li_2MnO_3 \cdot 0.45LiNi_{1/3}Co_{1/3}Mn_{1/3}O_2$ cathode for Li-ion batteries. *Electrochimica Acta* **2012,** *80*, 187-195.

12.   Sha, O.; Tang, Z.; Wang, S.; Yuan, W.; Qiao, Z.; Xu, Q.; Ma, L., The multi-substituted $LiNi_{0.475}Al_{0.01}Cr_{0.04}Mn_{1.475}O_{3.95}F_{0.05}$ cathode material with excellent rate capability

and cycle life. *Electrochimica Acta* **2012,** *77*, 250-255.

13.   Kim, J.-H.; Park, M.-S.; Song, J.-H.; Byun, D.-J.; Kim, Y.-J.; Kim, J.-S., Effect of aluminum fluoride coating on the electrochemical and thermal properties of 0.5Li2MnO3·0.5LiNi0.5Co0.2Mn0.3O2 composite material. *Journal of Alloys and Compounds* **2012,** *517*, 20-25.

14.   Shi, S. J.; Tu, J. P.; Tang, Y. Y.; Liu, X. Y.; Zhang, Y. Q.; Wang, X. L.; Gu, C. D., Enhanced cycling stability of Li[Li0.2Mn0.54Ni0.13Co0.13]O2 by surface modification of MgO with melting impregnation method. *Electrochimica Acta* **2013,** *88*, 671-679.

15.   Deng, Y.; Liu, S.; Liang, X., Study of carbon surface-modified Li[Li0.2Mn0.54Ni0.13Co0.13]O2 for high-capacity lithium ion battery cathode. *Journal of Solid State Electrochemistry* **2012,** *17* (4), 1067-1075.

16.   Xu, K.; von Cresce, A., Interfacing electrolytes with electrodes in Li ion batteries. *Journal of Materials Chemistry* **2011,** *21* (27), 9849.

17.   Harada, T.; Ikeda, S.; Ng, Y. H.; Sakata, T.; Mori, H.; Torimoto, T.; Matsumura, M., Rhodium Nanoparticle Encapsulated in a Porous Carbon Shell as an Active Heterogeneous Catalyst for Aromatic Hydrogenation. *Advanced Functional Materials* **2008,** *18* (15), 2190-2196.

18.   Li, F.; Morris, M.; Chan, K.-Y., Electrochemical capacitance and ionic transport in the mesoporous shell of a hierarchical porous core–shell carbon structure. *Journal of Materials Chemistry* **2011,** *21* (24), 8880.

19.   Wang, S.; Xing, Y.; Xiao, C.; Wei, X.; Xu, H.; Zhang, S., Hollow carbon-shell/carbon-nanorod arrays for high performance Li-ion batteries and supercapacitors. *RSC Adv.* **2015,** *5* (11), 7959-7963.

20.   Winter, M.; Brodd, R. J., What Are Batteries, Fuel Cells, and Supercapacitors? *Chemical Reviews* **2004,** *104* (10), 4245-4270.

21.   Wang, Y.; Cao, G., Developments in Nanostructured Cathode Materials for High-Performance Lithium-Ion Batteries. *Advanced Materials* **2008,** *20* (12), 2251-2269.

22.   Dunn, B.; Kamath, H.; Tarascon, J. M., Electrical energy storage for the grid: a battery of choices. *Science* **2011,** *334* (6058), 928-35.

23.   Larcher, D.; Tarascon, J. M., Towards greener and more sustainable batteries for electrical energy storage. *Nat Chem* **2015,** *7* (1), 19-29.

24.   Choi, J. W.; Aurbach, D., Promise and reality of post-lithium-ion batteries with high energy densities. *Nature Reviews Materials* **2016,** *1* (4), 16013.

25.   Cheng, F.; Liang, J.; Tao, Z.; Chen, J., Functional materials for rechargeable batteries. *Adv Mater* **2011,** *23* (15), 1695-715.

26.   Scrosati, B.; Hassoun, J.; Sun, Y.-K., Lithium-ion batteries. A look into the future. *Energy & Environmental Science* **2011,** *4* (9), 3287.

27.   Xu, K., Nonaqueous Liquid Electrolytes for Lithium-Based Rechargeable Batteries. *Chemical Reviews* **2004,** *104* (10), 4303-4418.

28.   Yi, T.-F.; Mei, J.; Zhu, Y.-R., Key strategies for enhancing the cycling stability and rate capacity of LiNi0.5Mn1.5O4 as high-voltage cathode materials for high power lithium-ion batteries. *Journal of Power Sources* **2016,** *316*, 85-105.

29.   Zhang, X.; Belharouak, I.; Li, L.; Lei, Y.; Elam, J. W.; Nie, A.; Chen, X.; Yassar, R. S.; Axelbaum, R. L., Structural and Electrochemical Study of Al2O3and TiO2Coated Li1.2Ni0.13Mn0.54Co0.13O2Cathode Material Using ALD. *Advanced Energy Materials* **2013,** *3* (10), 1299-1307.

30.   Kim, J.-M.; Park, C.-H.; Wu, Q.; Lee, S.-Y., 1D Building Blocks-Intermingled Heteronanomats as a Platform Architecture For High-Performance Ultrahigh-Capacity Lithium-Ion Battery Cathodes. *Advanced Energy Materials* **2016,** *6* (2), 1501594.

31.   Zhang, X.; Cheng, F.; Yang, J.; Chen, J., LiNi(0.5)Mn(1.5)O4 porous nanorods as high-rate and long-life cathodes for Li-ion batteries. *Nano Lett* **2013,** *13* (6), 2822-5.

32.   Zhou, L.; Zhao, D.; Lou, X., LiNi(0.5)Mn(1.5)O4 hollow structures as high-performance cathodes for lithium-ion batteries. *Angew Chem Int Ed Engl* **2012,** *51* (1), 239-41.

33.   Zhang, S. S., A review on electrolyte additives for lithium-ion batteries. *Journal of Power Sources* **2006,** *162* (2), 1379-1394.

34.   Zhang, L.; Huang, J.; Youssef, K.; Redfern, P. C.; Curtiss, L. A.; Amine, K.; Zhang, Z., Molecular Engineering toward Stabilized Interface: An Electrolyte Additive for High-Performance Li-Ion Battery. *Journal of the Electrochemical Society* **2014,** *161* (14), A2262-A2267.

35.   Chung, S. Y.; Bloking, J. T.; Chiang, Y. M., Electronically conductive phospho-olivines as lithium storage electrodes. *Nat Mater* **2002,** *1* (2), 123-8.

36.   Fisher, C. A. J.; Hart Prieto, V. M.; Islam, M. S., Lithium Battery Materials LiMPO4(M= Mn, Fe, Co, and Ni): Insights into Defect Association, Transport Mechanisms, and Doping Behavior. *Chemistry of Materials* **2008,** *20* (18), 5907-5915.

37.   Fergus, J. W., Recent developments in cathode materials for lithium ion batteries. *Journal of Power Sources* **2010,** *195* (4), 939-954.

38.   Li, C.; Zhang, H. P.; Fu, L. J.; Liu, H.; Wu, Y. P.; Rahm, E.; Holze, R.; Wu, H. Q., Cathode materials modified by surface coating for lithium ion batteries. *Electrochimica Acta* **2006,** *51* (19), 3872-3883.

39.   Myung, S.-T.; Amine, K.; Sun, Y.-K., Surface modification of cathode materials from nano- to microscale for rechargeable lithium-ion batteries. *Journal of Materials Chemistry* **2010,** *20* (34), 7074.

40.   Cho, J.-H.; Park, J.-H.; Lee, M.-H.; Song, H.-K.; Lee, S.-Y., A polymer electrolyte-skinned active material strategy toward high-voltage lithium ion batteries: a polyimide-coated LiNi0.5Mn1.5O4 spinel cathode material case. *Energy & Environmental Science* **2012,** *5* (5), 7124.

41.   Wang, B.; Liu, T.; Liu, A.; Liu, G.; Wang, L.; Gao, T.; Wang, D.; Zhao, X. S., A Hierarchical Porous C@LiFePO4/Carbon Nanotubes Microsphere Composite for High-Rate Lithium-Ion Batteries: Combined Experimental and Theoretical Study. *Advanced Energy Materials* **2016,** *6* (16), 1600426.

42.   Li, X.; Zhang, Z.; Li, S.; Yang, L.; Hirano, S.-i., Polymeric ionic liquid-plastic crystal composite electrolytes for lithium ion batteries. *Journal of Power Sources* **2016,** *307*, 678-683.

43.   Ye, Y.-S.; Wang, H.; Bi, S.-G.; Xue, Y.; Xue, Z.-G.; Zhou, X.-P.; Xie, X.-L.; Mai, Y.-W., High performance composite polymer electrolytes using polymeric ionic liquid-functionalized graphene molecular brushes. *J. Mater. Chem. A* **2015,** *3* (35), 18064-18073.

44.   Ayalneh Tiruye, G.; Muñoz-Torrero, D.; Palma, J.; Anderson, M.; Marcilla, R., All-solid state supercapacitors operating at 3.5 V by using ionic liquid based polymer electrolytes. *Journal of Power Sources* **2015,** *279*, 472-480.

45.   Zhang, S.; Dokko, K.; Watanabe, M., Direct Synthesis of Nitrogen-Doped Carbon Materials from Protic Ionic Liquids and Protic Salts: Structural and Physicochemical Correlations between Precursor and Carbon. *Chemistry of Materials* **2014,** *26* (9), 2915-2926.

46.   Ambrogi, M.; Sakaushi, K.; Antonietti, M.; Yuan, J., Poly(ionic liquid)s for enhanced activation of cotton to generate simple and cheap fibrous electrodes for energy applications. *Polymer* **2015,** *68*, 315-320.

47.   Wang, X.; Li, J.; Chen, G.; Guo, Z.; Zhou, Y.; Wang, J., Hydrophobic Mesoporous Poly(ionic liquid)s towards Highly Efficient and Contamination-Resistant Solid-Base Catalysts. *ChemCatChem* **2015,** *7* (6), 993-1003.

48.   Marcilla, R.; Curri, M. L.; Cozzoli, P. D.; Martinez, M. T.; Loinaz, I.; Grande, H.; Pomposo, J. A.; Mecerreyes, D., Nano-objects on a round trip from water to organics in a

polymeric ionic liquid vehicle. *Small* **2006,** *2* (4), 507-12.

49.   Marcilla, R.; Blazquez, J. A.; Fernandez, R.; Grande, H.; Pomposo, J. A.; Mecerreyes, D., Synthesis of Novel Polycations Using the Chemistry of Ionic Liquids. *Macromolecular Chemistry and Physics* **2005,** *206* (2), 299-304.

50.   Marcilla, R.; Alberto Blazquez, J.; Rodriguez, J.; Pomposo, J. A.; Mecerreyes, D., Tuning the solubility of polymerized ionic liquids by simple anion-exchange reactions. *Journal of Polymer Science Part A: Polymer Chemistry* **2004,** *42* (1), 208-212.

51.   Mi, H.; Jiang, Z.; Kong, J., Hydrophobic Poly(ionic liquid) for Highly Effective Separation of Methyl Blue and Chromium Ions from Water. *Polymers* **2013,** *5* (4), 1203-1214.

52.   Marcilla, R.; Ochoteco, E.; Pozo-Gonzalo, C.; Grande, H.; Pomposo, J. A.; Mecerreyes, D., New Organic Dispersions of Conducting Polymers Using Polymeric Ionic Liquids as Stabilizers. *Macromolecular Rapid Communications* **2005,** *26* (14), 1122-1126.

53.   Singh, M. K.; Agarwal, A.; Gopal, R.; Swarnkar, R. K.; Kotnala, R. K., Dumbbell shaped nickel nanocrystals synthesized by a laser induced fragmentation method. *Journal of Materials Chemistry* **2011,** *21* (30), 11074.

54.   Zhao, L.; Hu, Y. S.; Li, H.; Wang, Z.; Chen, L., Porous Li4 Ti5 O12 coated with N-doped carbon from ionic liquids for Li-ion batteries. *Adv Mater* **2011,** *23* (11), 1385-8.

55.   Kumar, B.; Asadi, M.; Pisasale, D.; Sinha-Ray, S.; Rosen, B. A.; Haasch, R.; Abiade, J.; Yarin, A. L.; Salehi-Khojin, A., Renewable and metal-free carbon nanofibre catalysts for carbon dioxide reduction. *Nature Communications* **2013,** *4*.

56.   Lockett, V.; Sedev, R.; Harmer, S.; Ralston, J.; Horne, M.; Rodopoulos, T., Orientation and mutual location of ions at the surface of ionic liquids. *Phys Chem Chem Phys* **2010,** *12* (41), 13816-27.

57.   Keppler, A.; Himmerlich, M.; Ikari, T.; Marschewski, M.; Pachomow, E.; Hofft, O.; Maus-Friedrichs, W.; Endres, F.; Krischok, S., Changes of the near-surface chemical composition of the 1-ethyl-3-methylimidazolium bis(trifluoromethylsulfonyl)imide room temperature ionic liquid under the influence of irradiation. *Phys Chem Chem Phys* **2011,** *13* (3), 1174-81.

58.   Li, H.; Shen, L.; Yin, K.; Ji, J.; Wang, J.; Wang, X.; Zhang, X., Facile synthesis of N-doped carbon-coated Li4Ti5O12 microspheres using polydopamine as a carbon source for high rate lithium ion batteries. *Journal of Materials Chemistry A* **2013,** *1* (24), 7270.

59.   Ding, Z.; Zhao, L.; Suo, L.; Jiao, Y.; Meng, S.; Hu, Y. S.; Wang, Z.; Chen, L., Towards understanding the effects of carbon and nitrogen-doped carbon coating on the electrochemical

performance of Li4Ti5O12 in lithium ion batteries: a combined experimental and theoretical study. *Phys Chem Chem Phys* **2011,** *13* (33), 15127-33.

60.   Liang, J.; Jiao, Y.; Jaroniec, M.; Qiao, S. Z., Sulfur and nitrogen dual-doped mesoporous graphene electrocatalyst for oxygen reduction with synergistically enhanced performance. *Angew Chem Int Ed Engl* **2012,** *51* (46), 11496-500.

61.   Dresselhaus, M. S.; Dresselhaus, G.; Jorio, A.; Souza Filho, A. G.; Saito, R., Raman spectroscopy on isolated single wall carbon nanotubes. *Carbon* **2002,** *40* (12), 2043-2061.

62.   Ren, Y.; Ma, Z.; Morris, R. E.; Liu, Z.; Jiao, F.; Dai, S.; Bruce, P. G., A solid with a hierarchical tetramodal micro-meso-macro pore size distribution. *Nat Commun* **2013,** *4*, 2015.

63.   Dees, D. W.; Kawauchi, S.; Abraham, D. P.; Prakash, J., Analysis of the Galvanostatic Intermittent Titration Technique (GITT) as applied to a lithium-ion porous electrode. *Journal of Power Sources* **2009,** *189* (1), 263-268.

64.   Kim, J. M.; Park, J. H.; Lee, C. K.; Lee, S. Y., Multifunctional semi-interpenetrating polymer network-nanoencapsulated cathode materials for high-performance lithium-ion batteries. *Sci Rep* **2014,** *4*, 4602.

65.   Lux, S. F.; Lucas, I. T.; Pollak, E.; Passerini, S.; Winter, M.; Kostecki, R., The mechanism of HF formation in LiPF6 based organic carbonate electrolytes. *Electrochemistry Communications* **2012,** *14* (1), 47-50.

66.   Kim, J.-H.; Kim, J.-H.; Kim, J.-M.; Lee, Y.-G.; Lee, S.-Y., Superlattice Crystals-Mimic, Flexible/Functional Ceramic Membranes: Beyond Polymeric Battery Separators. *Advanced Energy Materials* **2015,** *5* (24), 1500954.

67.   Jang, Y.-R.; Kim, J.-M.; Lee, J.-H.; Cho, S.-J.; Kim, G.; Ju, Y.-W.; Yeon, S.-H.; Yoo, J.; Lee, S.-Y., Molecularly designed, dual-doped mesoporous carbon/SWCNT nanoshields for lithium battery electrode materials. *J. Mater. Chem. A* **2016,** *4* (39), 14996-15005.